

The instability of a sedimenting suspension of weakly flexible fibres

Harishankar Manikantan¹, Lei Li², Saverio E. Spagnolie² and David Saintillan^{1,†}

¹Department of Mechanical and Aerospace Engineering, University of California San Diego, 9500 Gilman Drive, San Diego, CA 92093, USA

²Department of Mathematics, University of Wisconsin–Madison, 480 Lincoln Drive, Madison, WI 53706, USA

(Received 22 April 2014; revised 2 July 2014; accepted 15 August 2014)

Suspensions of sedimenting slender fibres in a viscous fluid are known to be unstable to fluctuations of concentration. In this paper we develop a theory for the role of fibre flexibility in sedimenting suspensions in the asymptotic regime of weakly flexible bodies (large elasto-gravitation number). Unlike the behaviour of straight fibres, individual flexible filaments rotate as they sediment, leading to an anisotropic base state of fibre orientations in an otherwise homogeneous suspension. A mean-field theory is derived to describe the evolution of fibre concentration and orientation fields, and we explore the stability of the base state to perturbations of fibre concentration. We show that fibre flexibility affects suspension stability in two distinct and competing ways: the anisotropy of the base state renders the suspension more unstable to perturbations, while individual particle self-rotation acts to prevent clustering and stabilizes the suspension. In the presence of thermal noise, the dominant effect depends critically upon the relative scales of flexible fibre self-rotation compared to rotational Brownian motion.

Key words: instability, low-Reynolds-number flows, suspensions

1. Introduction

The sedimentation of a suspension of particles in a viscous fluid at low Reynolds number is marked by long-range hydrodynamic interactions resulting in strong velocity fluctuations. This slowly decaying nature of multi-body interactions readily complicates even the seemingly simple case of a random dilute dispersion of sedimenting spheres (Guazzelli & Hinch 2011). The disturbance velocity at a distance r induced by a sphere decays as $1/r$, and a naive pairwise summation of the contributions of all spheres promptly leads to a diverging value of the settling velocity. This issue was first addressed by Batchelor (1972), who noted that, in a finite-sized container, the presence of a bottom wall in fact results in a vertical backflow that cancels the diverging part of the settling velocity; this can alternatively be perceived as the effect of a modified pressure field, the gradient of which balances

† Email address for correspondence: dstn@ucsd.edu

the weight of the suspension. While this observation resolved the problem with the mean settling speed, the variance of the particle velocities was later shown, in what has illustriously become known as the Caffisch–Luke paradox (Caffisch & Luke 1985; Ramaswamy 2001; Guazzelli & Hinch 2011), to increase unboundedly with system size, notwithstanding Batchelor’s renormalization. Such a divergence is not supported by experimental observations (Segrè, Herbolzheimer & Chaikin 1997; Bergougnoux *et al.* 2001; Guazzelli 2001), and various mechanisms have been suggested over the years to resolve this oddity, each with experiments and numerical simulations to support and challenge the notion. These mechanisms have included the hydrodynamic screening of long-range interactions as a result of local microstructural changes (Koch & Shaqfeh 1991) or by vertical no-slip walls (Brenner 1999), homogenization of the suspension due to recirculating currents induced by horizontal boundaries (Hinch 1987; Ladd 2002), and the damping of fluctuations by vertical density gradients (Luke 2000; Mucha *et al.* 2004).

The suspension microstructure becomes all the more important in the case of anisotropic particles. Consider for the moment a collection of rigid spheroids of a defined geometry, with the configuration of each particle now specified by its position and orientation. While the contribution of particle geometry to the aforementioned effects is not obvious *a priori*, we can readily see that such a dispersion is fundamentally different from one containing only spherical particles in that spheroids can orient in flow. This orientation, in turn, decides the direction of sedimentation, which no longer has to be vertically downwards even in the case of a single particle in a quiescent fluid. This simple consequence of viscous drag anisotropy has been well studied, and knowledge of the hydrodynamic mobilities along and perpendicular to the particle major axis lets one evaluate its settling velocity. At a suspension level, this dependence of particle velocities on their orientations seriously complicates the dynamics, as the disturbance velocity field in the suspension can now reorient particles and hence dramatically affect their trajectories over large length scales. This problem was first studied by Koch & Shaqfeh (1989), who modelled a dilute suspension of rigid spheroids using a Smoluchowski equation for the continuous probability field of particle positions and orientations. Perturbing around a spatially homogeneous and orientationally isotropic base-state distribution, they predicted a linear concentration instability in which perturbations with the longest wavelengths are the most unstable. In short, the mechanism is as follows: hydrodynamic interactions cause denser particle clusters to sediment faster than their surroundings, inducing a disturbance field that orients neighbouring particles in such a way that they preferentially migrate towards the already dense clusters, thereby amplifying the concentration fluctuations.

The instability predicted by Koch & Shaqfeh (1989) has been amply confirmed by experiments on rigid fibres (Herzhaft *et al.* 1996; Metzger, Guazzelli & Butler 2005; Metzger, Butler & Guazzelli 2007) and by numerical simulations with various levels of sophistication (Butler & Shaqfeh 2002; Kuusela, Lahtinen & Ala-Nissila 2003; Saintillan, Darve & Shaqfeh 2005; Saintillan, Shaqfeh & Darve 2006*b*; Tornberg & Gustavsson 2006; Gustavsson & Tornberg 2009). More complex theoretical models have also been developed to address issues such as the effects of stratification in finite-sized containers (Saintillan, Shaqfeh & Darve 2006*a*), particle alignment under electric fields (Saintillan, Shaqfeh & Darve 2006*c*), Brownian fluctuations (Hoffman & Shaqfeh 2009) and fluid inertia (Dahlkild 2011; Zhang, Dahlkild & Lundell 2013). In all cases, the key ingredient remains the lateral migration due to the orientability of the anisotropic particles at the micromechanical level, and a suspension of rigid spheres is indeed stable to concentration fluctuations as elucidated

by Koch & Shaqfeh (1989) using the same linear stability analysis. Suspensions of isotropic particles, however, can exhibit an instability if the particles are allowed to deform and become anisotropic under flow (Saintillan *et al.* 2006*b*), as in the sedimentation of emulsions (Manga & Stone 1995; Zinchenko & Davis 2003). More generally, suspensions of isotropic particles have also been found to be unstable due to other types of nonlinear couplings between the direction of sedimentation of the particles and the local disturbance flow field that they induce, for instance due to Marangoni stresses in suspensions of spherical bubbles covered with surfactants (Narsimhan & Shaqfeh 2010), or to viscoelastic stresses in suspensions of rigid spheres in non-Newtonian fluids (Vishnampet & Saintillan 2012).

In this paper, we address the effects of fibre (or filament, as we shall use interchangeably in the rest of the paper) flexibility. Elastic filaments play crucial roles in many biological and technological processes: be it in fortifying cells in the form of biopolymers (Gardel *et al.* 2006), rendering locomotive capabilities to microorganisms (Lauga & Powers 2009), facilitating mammalian reproduction (Fauci & Dillon 2006), constituting the microstructure responsible for non-Newtonian behaviour of complex fluids (Bird, Armstrong & Hassager 1987), or permitting chaotic mixing (Groisman & Steinberg 2000), among numerous others. When a flexible filament is placed in a flow, the competition between viscous and elastic forces can result in complex deformations and dynamics at the particle level (Tornberg & Shelley 2004), and in turn drive drastic bulk behavioural changes at the macroscopic level (Switzer & Klingenberg 2003). Of particular relevance within the scope of this paper is the limit of weak flexibility where the filament departs only slightly from its straightened state. This regime is realized in many physical systems involving stiff polymers, carbon nanotubes, rod-like bacteria or microtubules. While it is a useful and often illustrative simplification to neglect fibre compliance completely in such systems (Saintillan & Shelley 2012; Gao *et al.* 2014), even weak flexibility has been shown to change the rheology (Keshtkar, Heuzey & Carreau 2009) and phase behaviour (Van Der Schoot 1996) of flexible fibre suspensions.

Pertinent to the present context is the fact that a compliant filament breaks the symmetry enjoyed by a rigid rod and is therefore susceptible to an additional coupling between translational and rotational motions. Under sedimentation, this leads to a new mechanism for fibre reorientation and, owing to drag anisotropy, to a change in the direction and magnitude of the settling velocity. There is no reason to expect steady and trivial trajectories any longer, as was previously illustrated by Xu & Nadim (1994) and Cosentino Lagomarsino, Pagonabarraga & Lowe (2005), who predicted that flexible fibres should spontaneously align perpendicular to gravity. Such reorientation dynamics and structural deformations were also reported in suspensions of filaments made of superparamagnetic colloids (Goubault *et al.* 2003) and electrophoretically driven microtubules (Van den Heuvel *et al.* 2008), the role of gravity in these cases being played by magnetic and electric fields, respectively.

In our recent work (Li *et al.* 2013), we applied slender-body theory and a multiple-scale asymptotic analysis to theoretically describe, and verify using numerical simulations, the reorientation dynamics and shape evolution of a single flexible fibre undergoing sedimentation. The key result that we shall exploit vastly in the current study is that, in the absence of flow or Brownian motion, the only stable orientation for the filament is one perpendicular to the direction of gravity, and every other configuration reorients at a rate that depends on flexural rigidity and instantaneous orientation. The notion of weak flexibility can be defined more precisely in terms of

an elasto-gravitation number β comparing elastic forces acting on the filament to the external gravitational force:

$$\beta = \frac{\pi E a^4}{4 F_G L^2} = \frac{\kappa}{F_G L^2}. \quad (1.1)$$

Here, the filament is assumed to be of a spheroidal geometry with length L and width $2a$ at its thickest point, F_G is the net gravitational force acting on it, E is the elastic modulus of the material that comprises the filament, and $\kappa = \pi E a^4 / 4$ is the bending stiffness. The regime of weak flexibility then corresponds to the limit of $\beta \gg 1$ and in this case the deviation of a sedimenting filament from its straightened state is $O(\beta^{-1})$. To leading order, the configuration of the filament in three dimensions is fully described by the position and tangential orientation of its centre, which in turn determines its deflection. As shown by Li *et al.* (2013), such a filament translates at the same velocity as a rigid rod, i.e.

$$\mathbf{u}_s(\mathbf{p}) = (\lambda_1 \mathbf{I} + \lambda_2 \mathbf{p}\mathbf{p}) \cdot \frac{\mathbf{F}_G}{8\pi\mu L} + O(\beta^{-2}), \quad (1.2)$$

where \mathbf{p} is a unit vector tangent to the filament at its centre, and μ is the viscosity of the suspending fluid. The filament also reorients as a result of flexibility at an angular velocity given by

$$\dot{\mathbf{p}}_s(\mathbf{p}) = \frac{F_G}{8\pi\mu L^2} \frac{A}{2\beta} \sin(2\theta) \hat{\boldsymbol{\theta}} + O(\beta^{-2}), \quad (1.3)$$

where $\theta = \cos^{-1}(\mathbf{p} \cdot \hat{\mathbf{z}})$ is the instantaneous angle made by the fibre with gravity and $\hat{\boldsymbol{\theta}}$ is the corresponding polar unit vector in spherical coordinates. The constants λ_1 , λ_2 and A are geometric factors given by $c + 1$, $c - 3$ and $3(c - 7/2)/80$, respectively, where $c = \ln(1/\epsilon^2)$ with $\epsilon = a/L$ the particle aspect ratio. Clearly, the changing orientation of the filament affects its speed and direction of sedimentation, leading to non-trivial trajectories. As can be seen from (1.3), the filament tends to align perpendicular to gravity, after which a quasi-steady state is achieved with steady vertical downward translation. The deflection of the filament was also calculated by Li *et al.* (2013), with a maximum value of $L/256\beta$ attained at steady state. For a slender filament of aspect ratio $\epsilon = 0.01$, we find that the maximum deflection is approximately $0.004L$ when $\beta = 1$. This suggests that, to an excellent approximation, a stiff sedimenting filament behaves like a rigid rod with the added dynamics of reorientation and, through it, a non-constant sedimentation velocity. When multiple such filaments are allowed to interact hydrodynamically in a suspension, we expect the tendency to align horizontally to compete with the rotation of the particles in the disturbance flow they generate, with non-trivial consequences for the stability of the suspension as we analyse in this work.

The paper is organized as follows. In §2, we describe a simple model for the sedimentation of a collection of hydrodynamically interacting weakly flexible fibres, and use it to derive a mean-field theory for the evolution of the distribution of particle positions and orientations in a large-scale suspension. As we shall see, this mean-field continuum model admits a steady uniform base state that is anisotropic in orientation space and depends on fibre flexibility. The stability of the system to spatial perturbations around this base state is then analysed in §3, where we

find that flexibility affects the stability in two distinct ways. On the one hand, the anisotropic base state is shown to render the suspension more unstable as compared to a suspension of rigid rods; on the other hand, reorientation of the weakly flexible fibres under gravity can act to prevent clustering and stabilize the suspension by competing against rotation in the disturbance flow driven by density fluctuations. We conclude with a discussion in § 4.

2. Theoretical formulation

In this section, we formulate a theoretical model for the dynamics in a suspension of weakly flexible filaments sedimenting under gravity. We first present a simple micromechanical model for a discrete collection of filaments in § 2.1. This simple model is then used in § 2.2 as the basis for a mean-field continuum theory that extends the model of Koch & Shaqfeh (1989) to account for the leading effects of weak flexibility.

2.1. Micromechanical model

As rationalized in the discussion of the previous section, we model a dilute suspension of weakly flexible fibres using rigid-rod dynamics, with flexibility entering only through an additional component to the rotational velocity. The instantaneous centre-of-mass position and orientation of particle α in the suspension are given by $\mathbf{x}_\alpha = (x_\alpha, y_\alpha, z_\alpha)$ and $\mathbf{p}_\alpha = (\sin \theta_\alpha \cos \varphi_\alpha, \sin \theta_\alpha \sin \varphi_\alpha, \cos \theta_\alpha)$, where $\theta_\alpha \in [0, \pi]$ and $\varphi_\alpha \in [0, 2\pi)$ denote the polar and azimuthal angles on the unit sphere of orientations Ω , respectively. We take gravity to be in the $-\hat{z}$ direction. In a dilute system and in the weakly flexible limit, the centre-of-mass velocity of fibre α is modelled as the sum of its settling velocity obtained in (1.2) and of the disturbance velocity \mathbf{u}_d induced in the fluid by the motion of the other fibres:

$$\dot{\mathbf{x}}_\alpha = \mathbf{u}_s(\mathbf{p}_\alpha) + \mathbf{u}_d(\mathbf{x}_\alpha). \tag{2.1}$$

Similarly, its angular velocity also includes contributions from sedimentation and from the disturbance flow, i.e.

$$\dot{\mathbf{p}}_\alpha = \dot{\mathbf{p}}_s(\mathbf{p}_\alpha) + \dot{\mathbf{p}}_d(\mathbf{x}_\alpha, \mathbf{p}_\alpha), \tag{2.2}$$

where $\dot{\mathbf{p}}_s(\mathbf{p}_\alpha)$ is given by (1.3) and accounts for the leading-order effect of flexibility. Particle reorientation due to the disturbance flow is modelled following Jeffery (1922) as

$$\dot{\mathbf{p}}_d(\mathbf{x}_\alpha, \mathbf{p}_\alpha) = (\mathbf{I} - \mathbf{p}_\alpha \mathbf{p}_\alpha) \cdot [\gamma \mathbf{E}_d(\mathbf{x}_\alpha) + \mathbf{W}_d(\mathbf{x}_\alpha)] \cdot \mathbf{p}_\alpha \tag{2.3}$$

in terms of the disturbance rate-of-strain tensor $\mathbf{E}_d = (\nabla_x \mathbf{u}_d + \nabla_x \mathbf{u}_d^T)/2$ and rate-of-rotation tensor $\mathbf{W}_d = (\nabla_x \mathbf{u}_d - \nabla_x \mathbf{u}_d^T)/2$, respectively, having chosen the convention that $(\nabla_x \mathbf{u})_{ij} = \partial u_i / \partial x_j$. In (2.3), $\gamma = (1 - 4\epsilon^2)/(1 + 4\epsilon^2)$ is a measure of particle anisotropy, and we take $\gamma \approx 1$ in this work, corresponding to the limit of very slender fibres. It should be noted that (2.1)–(2.3) technically describe the motion of a fibre in a linear flow field. They are expected to hold in dilute suspensions where spatial variations of the disturbance field occur on length scales much greater than the particle dimensions, and could be corrected to account for small-scale velocity fluctuations using more general Faxén relations for spheroidal particles in arbitrary flows (Kim & Karrila 2005).

Integration of (2.1) and (2.2) requires knowledge of the disturbance velocity induced in the fluid by the other particles. This disturbance velocity arises from the net gravitational force on each fibre, which is transmitted to the fluid. In the dilute limit and to leading order, the velocity experienced by particle α therefore solves the forced Stokes equations

$$-\mu \nabla_x^2 \mathbf{u}_d + \nabla_x q_d = \mathbf{F}_G \sum_{\beta \neq \alpha} \delta(\mathbf{x} - \mathbf{x}_\beta), \quad \nabla_x \cdot \mathbf{u}_d = 0. \quad (2.4a,b)$$

Here, $\delta(\mathbf{x})$ is the three-dimensional Dirac delta function, $q_d(\mathbf{x})$ is the disturbance pressure field set up by the flow, and we have assumed that the viscosity of the fluid is unaffected by the particles. Equations (2.4) also implicitly assume that particles are widely separated so that the effects of higher force moments on the particles are negligible compared to the flow induced by the net gravitational force. In the limit of rigid rods ($\beta \rightarrow \infty$ and $\dot{\mathbf{p}}_s \rightarrow \mathbf{0}$), the model posed here is identical to that used by Mackaplow & Shaqfeh (1998) in their discrete particle simulations.

2.2. Mean-field theory

Following Koch & Shaqfeh (1989), we now introduce a continuum mean-field theory based on the micromechanical model described above. Rather than tracking the motions of individual fibres, we describe the configuration of the suspension in terms of the probability distribution function $\Psi(\mathbf{x}, \mathbf{p}, t)$ of finding a particle at position \mathbf{x} with orientation \mathbf{p} at time t . The distribution function is normalized as

$$\frac{1}{V} \int_V \int_\Omega \Psi(\mathbf{x}, \mathbf{p}, t) \, d\mathbf{p} \, d\mathbf{x} = n, \quad (2.5)$$

where V is the volume of the suspension and n is the mean number density. Conservation of particles is expressed by the Smoluchowski equation (Doi & Edwards 1986)

$$\frac{\partial \Psi}{\partial t} + \nabla_x \cdot (\dot{\mathbf{x}} \Psi) + \nabla_p \cdot (\dot{\mathbf{p}} \Psi) - \nabla_x \cdot (\mathbf{D} \cdot \nabla_x \Psi) - \nabla_p \cdot (d \nabla_p \Psi) = 0, \quad (2.6)$$

where differential operators with a subscript x act on spatial coordinates while those with a subscript p act on the sphere of orientations, i.e.

$$\nabla_p \equiv (\mathbf{I} - \mathbf{p}\mathbf{p}) \cdot \frac{\partial}{\partial \mathbf{p}} = \hat{\boldsymbol{\theta}} \frac{\partial}{\partial \theta} + \frac{\hat{\boldsymbol{\phi}}}{\sin \theta} \frac{\partial}{\partial \phi}. \quad (2.7)$$

In (2.6), $\dot{\mathbf{x}}$ and $\dot{\mathbf{p}}$ denote the translational and rotational flux velocities. Based on the discussion of § 2.1, these include contributions from sedimentation and from the disturbance flow field \mathbf{u}_d in the suspension:

$$\dot{\mathbf{x}} = \mathbf{u}_s(\mathbf{p}) + \mathbf{u}_d(\mathbf{x}), \quad (2.8)$$

$$\dot{\mathbf{p}} = \dot{\mathbf{p}}_s(\mathbf{p}) + \dot{\mathbf{p}}_d(\mathbf{x}, \mathbf{p}). \quad (2.9)$$

Here $\mathbf{u}_s(\mathbf{p})$ and $\dot{\mathbf{p}}_s(\mathbf{p})$ were defined in (1.2) and (1.3), respectively, and $\dot{\mathbf{p}}_d(\mathbf{x}, \mathbf{p})$ is related to $\mathbf{u}_d(\mathbf{x})$ through Jeffery's equation (2.3). Equation (2.6) also accounts for translational and rotational diffusion with constant diffusivities \mathbf{D} and d . In this work,

we assume that these diffusivities arise primarily from Brownian motion and can be related via the Stokes–Einstein relation (Doi & Edwards 1986) to the translational and rotational mobilities of the particles obtained from slender-body theory,

$$\mathbf{D} = \frac{k_B T}{8\pi\mu L}(\lambda_1 \mathbf{I} + \lambda_2 \mathbf{p}\mathbf{p}), \quad d = \frac{k_B T \lambda_3}{8\pi\mu L^3}, \quad (2.10a,b)$$

where $\lambda_3 = 12(c - 1)$ and $k_B T$ is the thermal energy unit. More sophisticated models may be used for these diffusivities in the case of non-Brownian suspensions, where their origin is hydrodynamic rather than thermal (Ham & Homsy 1988; Mucha & Brenner 2003).

The above system is closed with a description of the mean-field disturbance velocity $\mathbf{u}_d(\mathbf{x})$. In the continuum limit, the forced Stokes equations (2.4) become

$$-\mu \nabla_x^2 \mathbf{u}_d + \nabla_x q_d = \mathbf{F}_G c(\mathbf{x}, t), \quad \nabla_x \cdot \mathbf{u}_d = 0, \quad (2.11)$$

where $c(\mathbf{x}, t)$ denotes the local concentration of particles and is obtained from the distribution function as

$$c(\mathbf{x}, t) = \int_{\Omega} \Psi(\mathbf{x}, \mathbf{p}, t) d\mathbf{p}. \quad (2.12)$$

The flow is driven by the forcing term on the right-hand side of the momentum equation, which can be interpreted as a body force acting on the fluid that is everywhere proportional to the local weight of the suspension. In the limit of rigid rods ($\beta \rightarrow \infty$ and $\dot{\mathbf{p}}_s \rightarrow \mathbf{0}$) and in the absence of diffusion ($\mathbf{D} = \mathbf{0}$ and $d = 0$), this continuum model reduces to the original model of Koch & Shaqfeh (1989) for a non-Brownian suspension of sedimenting rigid rods.

2.3. Homogeneous base-state distribution

We first seek a steady and spatially homogeneous solution $\Psi(\mathbf{x}, \mathbf{p}, t) = n \Psi_0(\mathbf{p})$ of the mean-field model in an infinite domain, which will serve as the base-state distribution for the linear stability analysis of §3. In this case, the body force in the Stokes equations (2.11) reduces to $n\mathbf{F}_G$, with an obvious solution given by

$$\mathbf{u}_d(\mathbf{x}) = \mathbf{0}, \quad q_d(\mathbf{x}) = -nF_G z + q_d^0. \quad (2.13a,b)$$

Therefore, in the absence of concentration fluctuations, the disturbance flow is zero and a hydrostatic pressure gradient balances the buoyant weight of the suspension. In this case, the Smoluchowski equation (2.6) simplifies to

$$\nabla_p \cdot (\dot{\mathbf{p}}_s \Psi_0) = d \nabla_p^2 \Psi_0, \quad (2.14)$$

expressing the balance of reorientation due to flexibility and rotational diffusion. We expect the base state to depend only on the inclination θ of the particles from $\hat{\mathbf{z}}$. This allows us to solve for Ψ_0 exactly as

$$\Psi_0(\theta) = m_0 \exp \left[-\frac{AF_G^2 L^3}{4k_B T \lambda_3 \kappa} \cos 2\theta \right], \quad (2.15)$$

where m_0 is a normalization constant, with $m_0 = (4\pi)^{-1}$ for an isotropic orientation distribution. Let us introduce the gravitational Péclet number Pe , or ratio of the gravitational potential to the thermal energy:

$$Pe = \frac{F_G L}{k_B T}. \quad (2.16)$$

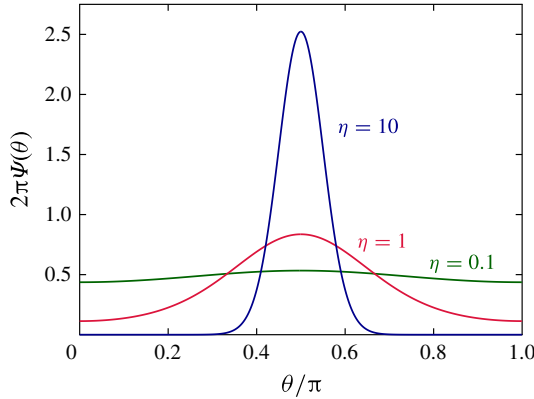


FIGURE 1. (Colour online) Anisotropic base-state orientation distribution $\Psi_0(\theta)$, given by (2.17), for different values of $\eta = A Pe/4\lambda_3\beta$. Flexibility causes particles to preferentially align in directions perpendicular to gravity.

The base-state distribution (2.15) can then be rewritten as

$$\Psi_0(\theta) = \frac{1}{2\pi} \frac{e^{-2\eta \cos^2 \theta}}{\int_{-1}^1 e^{-2\eta u^2} du}, \tag{2.17}$$

where we have defined $\eta = A Pe/4\lambda_3\beta$. As illustrated in figure 1, any amount of flexibility causes the fibres to align preferentially in the plane normal to the direction of gravity, and this tendency strengthens in the limits of weak rotational diffusion (large Pe) and of increasing flexibility (small β , although we recall that the micromechanical model is technically valid for $\beta \gtrsim 1$). Two limits of interest can be noted: if $\eta \ll 1$ the distribution is isotropic ($\Psi_0(\theta) \rightarrow (4\pi)^{-1}$), while if $\eta \gg 1$ all the filaments assume nearly horizontal orientations ($\Psi_0(\theta) \rightarrow \delta(\theta - \pi/2)/2\pi$). In the following, we shall explore the regime where $\eta \gtrsim O(1)$, and frequently return to the case of small η for comparison with the already established results for an isotropic suspension (Koch & Shaqfeh 1989).

3. Linear stability

3.1. Eigenvalue problem

We now perturb the system about the base-state distribution as $\Psi(\mathbf{x}, \mathbf{p}, t) = n[\Psi_0(\theta) + \varepsilon\psi'(\mathbf{x}, \mathbf{p}, t)]$, with $|\varepsilon| \ll 1$ and $|\psi'| \sim O(1)$. This weak perturbation in concentration leads to a weak disturbance velocity and an associated angular velocity: $\mathbf{u}_d = \varepsilon\mathbf{u}'_d$ and $\dot{\mathbf{p}}_d = \varepsilon\dot{\mathbf{p}}'_d$. Substituting these along with the base-state equation (2.17) into the conservation equation (2.6) and collecting terms of $O(\varepsilon)$, we obtain

$$\begin{aligned} \frac{\partial \psi'}{\partial t} + \nabla_x \psi' \cdot \mathbf{u}_s + \nabla_p \Psi_0 \cdot \dot{\mathbf{p}}'_d + \Psi_0 \nabla_p \cdot \dot{\mathbf{p}}'_d \\ + \nabla_p \psi' \cdot \dot{\mathbf{p}}_s + \psi' \nabla_p \cdot \dot{\mathbf{p}}_s - \nabla_x \cdot (\mathbf{D} \cdot \nabla_x \psi') - d \nabla_p^2 \psi' = 0. \end{aligned} \tag{3.1}$$

To proceed, we impose Fourier modes with wavevector \mathbf{k} and complex frequency $\omega = \omega_R + i\omega_I$ on the perturbed quantities, e.g. $\psi'(\mathbf{x}, \mathbf{p}, t) = \tilde{\psi}(\mathbf{k}, \mathbf{p}, \omega) \exp[i(\mathbf{k} \cdot \mathbf{x} - \omega t)]$.

In doing so, we are assuming that the fluid occupies all space, or, in the event that the fluid is contained, that the container is assumed to be large enough so that walls have negligible effects on the suspension dynamics. The disturbance velocity and angular velocity then accommodate similar normal modes due to the linearity of the Stokes equations. Following Hasimoto (1959), we know the velocity from (2.11) in Fourier space as

$$\tilde{\mathbf{u}}(\mathbf{k}, \mathbf{p}, \omega) = \frac{n}{\mu k^2} (\mathbf{I} - \hat{\mathbf{k}}\hat{\mathbf{k}}) \cdot \mathbf{F}_G \tilde{c}(\mathbf{k}, \omega), \tag{3.2}$$

with $\hat{\mathbf{k}} = \mathbf{k}/k$ and $k = |\mathbf{k}|$. Here, correspondingly, $c(\mathbf{x}, t) = n[1 + \varepsilon c'(\mathbf{x}, t)]$ and $c'(\mathbf{x}, t) = \tilde{c}(\mathbf{k}, \omega) \exp[i(\mathbf{k} \cdot \mathbf{x} - \omega t)]$, so that $\tilde{c} = \int_{\Omega} \tilde{\psi} \, d\mathbf{p}$. Then, using Jeffery’s equation (2.3), we find the Fourier coefficients of the angular velocity and its orientational divergence:

$$\tilde{\dot{\mathbf{p}}}(\mathbf{k}, \mathbf{p}, \omega) = i \frac{n}{\mu k^2} (\mathbf{p} \cdot \mathbf{k})(\mathbf{I} - \mathbf{p}\mathbf{p}) \cdot (\mathbf{I} - \hat{\mathbf{k}}\hat{\mathbf{k}}) \cdot \mathbf{F}_G \tilde{c}(\mathbf{k}, \omega), \tag{3.3}$$

$$\nabla_p \cdot \tilde{\dot{\mathbf{p}}}(\mathbf{k}, \mathbf{p}, \omega) = -3i \frac{n}{\mu k^2} (\mathbf{p} \cdot \mathbf{k})\mathbf{p} \cdot (\mathbf{I} - \hat{\mathbf{k}}\hat{\mathbf{k}}) \cdot \mathbf{F}_G \tilde{c}(\mathbf{k}, \omega). \tag{3.4}$$

Using $\mathbf{F}_G = -F_G \hat{\mathbf{z}}$ and the Fourier coefficients obtained in (3.2)–(3.4), the linearized conservation equation (3.1) simplifies to

$$\begin{aligned} &(-i\omega + i\mathbf{k} \cdot \mathbf{u}_s + \nabla_p \cdot \dot{\mathbf{p}}_s + \mathbf{k} \cdot \mathbf{D} \cdot \mathbf{k}) \tilde{\psi} - d \nabla_p^2 \tilde{\psi} + \dot{\mathbf{p}}_s \cdot \nabla_p \tilde{\psi} \\ &+ i \frac{n F_G}{\mu k^2} [3\Psi_0(\mathbf{p} \cdot \mathbf{k})\mathbf{p} \cdot (\mathbf{I} - \hat{\mathbf{k}}\hat{\mathbf{k}}) \cdot \hat{\mathbf{z}} - (\mathbf{p} \cdot \mathbf{k})\nabla_p \Psi_0 \cdot (\mathbf{I} - \mathbf{p}\mathbf{p}) \cdot (\mathbf{I} - \hat{\mathbf{k}}\hat{\mathbf{k}}) \cdot \hat{\mathbf{z}}] \tilde{c} = 0. \end{aligned} \tag{3.5}$$

For simplicity, we assume that $\hat{\mathbf{k}} \cdot \hat{\mathbf{z}} = 0$, as horizontal waves are known to be the most unstable in the case of rigid rods (Koch & Shaqfeh 1989). Equations (1.2) and (1.3) can be inserted for \mathbf{u}_s and $\dot{\mathbf{p}}_s$. After scaling lengths by the filament length L and time by the sedimentation time scale $8\pi\mu L^2/F_G$, we recast the above equation as

$$\begin{aligned} &\{-i\omega - i\mathbf{k} \cdot (\lambda_1 \mathbf{I} + \lambda_2 \mathbf{p}\mathbf{p}) \cdot \hat{\mathbf{z}} + A\beta^{-1}(3 \cos^2 \theta - 1) + Pe^{-1}[\lambda_1 k^2 + \lambda_2(\mathbf{p} \cdot \mathbf{k})^2]\} \tilde{\psi} \\ &- \lambda_3 Pe^{-1} \nabla_p^2 \tilde{\psi} + \frac{A}{2} \beta^{-1} \sin 2\theta \frac{\partial \tilde{\psi}}{\partial \theta} + i \mathcal{F} \tilde{c} = 0. \end{aligned} \tag{3.6}$$

Here, \mathcal{F} is a scalar function defined as

$$\mathcal{F} = \frac{\mathcal{N}}{k^2} [3\Psi_0(\mathbf{p} \cdot \mathbf{k})(\mathbf{p} \cdot \hat{\mathbf{z}}) - (\mathbf{p} \cdot \mathbf{k})\nabla_p \Psi_0 \cdot (\mathbf{I} - \mathbf{p}\mathbf{p}) \cdot \hat{\mathbf{z}}] \tag{3.7}$$

$$= -\frac{\mathcal{N}}{k^2} \nabla_p \cdot [\Psi_0(\mathbf{p} \cdot \mathbf{k})(\mathbf{I} - \mathbf{p}\mathbf{p}) \cdot \hat{\mathbf{z}}], \tag{3.8}$$

where $\mathcal{N} = 8\pi n L^3$ can be interpreted as an effective volume fraction. As previously noted by Koch & Shaqfeh (1989), the only intrinsic length scale of the problem at the suspension level is $(nL)^{-1/2}$. For the mean-field description used here to be valid, this length scale should be much greater than the particle size L , which implies that $nL^3 \ll 1$, consistent with the assumption of a dilute suspension. Another restriction arises from the use of (2.1) and (2.2) for the particle motions, which assume that the disturbance velocity field varies smoothly on the scale of the fibres. This condition limits the validity of the above model to Fourier perturbations such that $k^{-1} \gg L$.

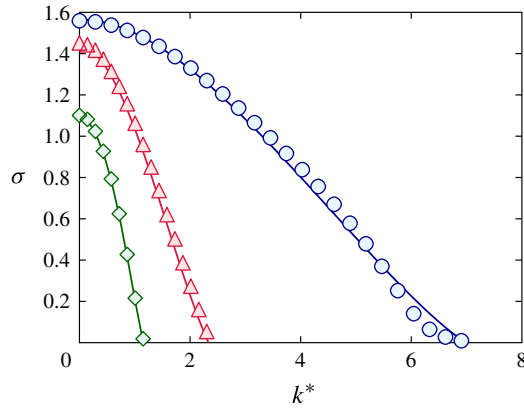


FIGURE 2. (Colour online) Spectral solution of the growth rate, σ , as a function of the horizontal perturbation wavenumber k^* , from (3.6), for $Pe = 10^6$ and $\beta = 1000$ (\diamond), 100 (\triangle) and 10 (\circ). The solid lines show the theoretical predictions of (3.25) for the base-state-driven instability for corresponding values of η , demonstrating that the leading effect of flexibility on the stability occurs primarily through the anisotropy of the base-state orientation distribution.

Equation (3.6) is an eigenvalue problem for the complex frequency ω , with corresponding eigenfunctions given by $\tilde{\psi}$. In the limit of rigid rods and negligible Brownian motion ($\beta, Pe \rightarrow \infty$ with $\eta \rightarrow 0$), it reduces to the eigenvalue problem previously obtained and solved by Koch & Shaqfeh (1989). It is interesting to note that flexibility and Brownian motion alter the problem in several distinct ways. First, they both have a direct influence through the terms involving β^{-1} and Pe^{-1} in (3.6), which capture rotation away from the direction of gravity as a result of flexibility and diffusive processes, respectively. In addition, they also both affect the base-state orientation distribution $\Psi_0(\theta)$ appearing in the function \mathcal{F} through the parameter $\eta = A Pe / 4\lambda_3\beta$ setting the degree of anisotropy as previously explained in § 2.3. As we shall show below, the direct and indirect effects of β and Pe are subtle and have non-trivial consequences for the stability. Before analysing successively the roles played by base-state anisotropy, flexibility and diffusion, we first discuss the full numerical solution of the eigenvalue problem (3.6) using a spectral method.

3.2. Spectral solution

Noting that (3.6) is an eigenvalue problem of the form $\mathcal{L}[\tilde{\Psi}] = i\omega\tilde{\Psi}$, where \mathcal{L} is a linear integro-differential operator, we first seek a spectral solution for the eigenvalues ω by projecting the eigenmodes $\tilde{\psi}$ on the basis of spherical harmonics as detailed in appendix A. The eigenvalue ω with the largest imaginary part ω_I decides the stability of the system. In figure 2, we plot the normalized growth rate $\sigma = \omega_I / \omega_m$ against the normalized wavenumber $k^* = k/k_m$ for different values of Pe and β . Here, the variables ω_m and k_m are, respectively, the zero-wavenumber growth rate and zero-growth-rate wavenumber for an isotropic suspension as in Saintillan *et al.* (2006a), and we shall asymptotically rederive them in § 3.3. As shown previously by Hoffman & Shaqfeh (2009) and confirmed by our numerical experiments, the leading effect of Brownian motion is to stabilize the system. Therefore, we first focus on the regime where Pe is large and hence the effects of diffusion are weak.

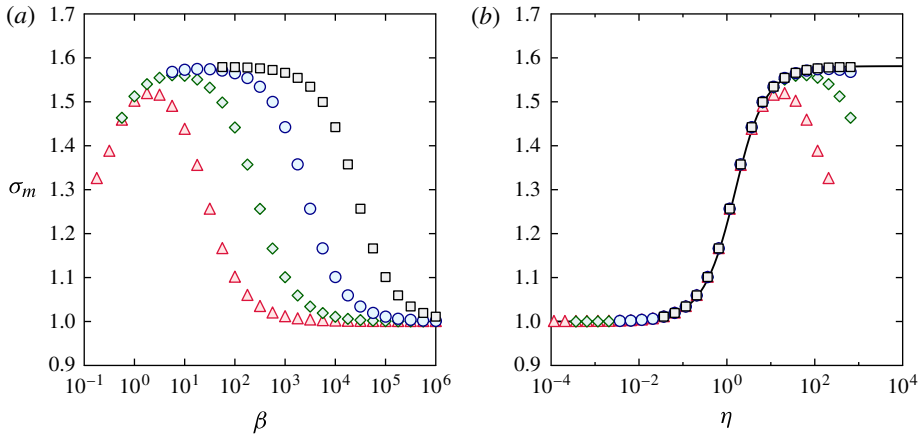


FIGURE 3. (Colour online) (a) Normalized growth rate at zero wavenumber for $Pe = 10^8$ (\square), 10^7 (\circ), 10^6 (\diamond) and 10^5 (\triangle) as obtained from the spectral solution. All cases asymptote to the isotropic rigid-rod limit as $\beta \rightarrow \infty$. (b) Same data scaled according to the parameter $\eta = A Pe / 4 \lambda_3 \beta$, with the predicted maximum growth rate (3.22) for the base-state-driven instability shown as a solid line.

The impact of flexibility in this case is clearly shown in figure 2. Here and in all spectral calculations shown below, we use the value of $\mathcal{N} = 1$ for the effective volume fraction, without affecting σ as will be shown. In the limit of stiff rods, obtained by letting $\beta \rightarrow \infty$ for finite Pe (and therefore $\eta \rightarrow 0$), the solution tends to the benchmark case previously analysed by Koch & Shaqfeh (1989) and Saintillan *et al.* (2006a), with a maximum growth rate of $\sigma = 1$ reached for $k^* = 0$. As the filaments become more flexible (i.e. as β decreases), both the range of unstable wavenumbers and the highest growth rate are observed to increase. In other words, we find that filament flexibility further destabilizes the perturbed suspension. Recall, however, that β cannot be arbitrarily small, as (1.3) for the angular velocity is valid only in the weakly flexible regime of $\beta \gtrsim 1$. Interestingly, the destabilization with decreasing β is found to be primarily the consequence of the indirect effect of flexibility on the anisotropy of the base state through (2.15), as the spectral solution to the full dispersion relation compares very well with an approximation (shown by the full lines in figure 2) that ignores the independent effects of Brownian motion and flexibility and only accounts for their contribution to the base state. This peculiar point and the physical mechanism for this base-state-driven destabilization will be addressed more precisely in § 3.3.

In figure 3(a), we look more closely at the dependence of the maximum growth rate $\sigma_m = \sigma(k^* = 0)$ on β and Pe , still focusing on the regime where the independent effect of Brownian motion is weak ($Pe \gtrsim 10^4$). The case of an isotropic suspension of rigid rods is recovered by letting $\beta \rightarrow \infty$ for all considered values of the Péclet number, as illustrated by a unique asymptote in the limit of large β . While all four curves for different values of Pe show similar shapes in this limit, we observe quite interestingly that the asymptote is approached faster with respect to β when the Péclet number is small. More precisely, an increase by a decade in Pe causes the range of β where the asymptote is approached also to increase by a decade, suggesting a self-similar dependence of the largest growth rate on Pe/β . This is confirmed in figure 3(b), showing the zero-wavenumber growth rates plotted versus η , where the values for all

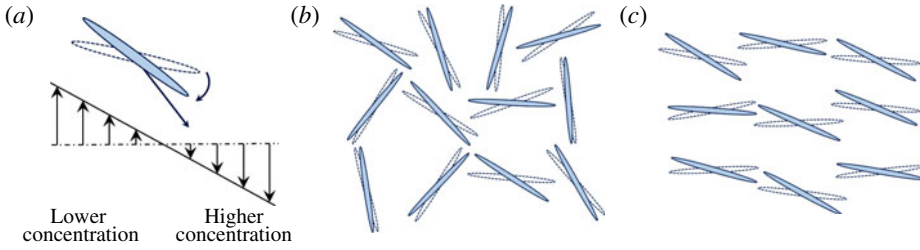


FIGURE 4. (Colour online) (a) Instability mechanism proposed by Koch & Shaqfeh (1989): the vertical shear flow set up by a horizontal density wave reorients particles such that they migrate preferentially towards high-concentration regions. (b) Effect of the vertical shear flow on an isotropic distribution: after a weak rotation, the distribution remains nearly isotropic, with only a weak net lateral migration towards the right. Empty shapes depict initial orientations in the base state, while filled ones represent orientations after rotation in the disturbance flow for a short duration. (c) Effect of the vertical shear flow on a strongly anisotropic orientation distribution: the weak rotation by the flow causes a large fraction of fibres to migrate towards the right, suggesting that base-state anisotropy can have a destabilizing effect on the suspension.

Pe and β collapse onto a single curve in the low- η range. This dependence on η , rather than on β and Pe independently, confirms that the dominant effect is that of the base state, and indeed we find that the self-similar curve matches an analytical prediction derived in §3.3 by neglecting the independent effects of flexibility and diffusion. As η exceeds unity, self-similarity is no longer observed, and figure 3(b) shows an eventual stabilization with decreasing β (or increasing η for a fixed Pe), presumably as a result of the independent effect of flexibility that competes against particle alignment by the flow and therefore hinders the growth of fluctuations.

3.3. Effect of the base state

As demonstrated by the full spectral solution in §3.2, both flexibility and Brownian motion primarily impact the stability by controlling the degree of anisotropy of the base state, and it is this effect that we further analyse here. The original instability mechanism proposed by Koch & Shaqfeh (1989) for an isotropic suspension of rigid rods is illustrated in figure 4(a). The key point is that a plane-wave perturbation in the number density sets up a vertical shear flow that causes neighbouring particles to reorient so that they sediment preferentially towards the regions of higher concentration, thereby bolstering the initial density fluctuation. This is a direct consequence of the shape anisotropy of the particles and of their ability to orient in the disturbance flow. This effect was further illustrated by Saintillan *et al.* (2006a), who considered an anisotropic base state given by an Onsager distribution. In contrast with the current work, they considered a distribution with a preferred orientation parallel to the direction of gravity, and found that the weak horizontal drift of the nearly vertical fibres led to a decrease in the growth rate of the instability. However, as illustrated in figure 4(b,c), the base state in the present study favours the direction perpendicular to gravity when $\eta > 0$, and this configuration increases the probability for a fibre to migrate towards the denser regions after a weak rotation by the disturbance flow. Thus, we expect the anisotropy of the base state to enhance the concentration instability in this case.

We restrict our attention here to the regime where both Brownian motion and filament flexibility are weak, i.e. $Pe^{-1} \ll 1$ and $\beta^{-1} \ll 1$. Notice that, in the limiting case, we require for a well-defined base state that both Pe and β tend to infinity at the same rate, so that η remains finite but arbitrary. Then, the leading-order terms in (3.6) for the eigenfunctions $\tilde{\psi} = \tilde{\psi}_0 + O(\beta^{-1}, Pe^{-1})$ and eigenvalues $\omega = \omega_0 + O(\beta^{-1}, Pe^{-1})$ become

$$\tilde{\psi}_0 = \frac{\mathcal{F} \tilde{c}_0}{\omega_0 + \lambda_2(\mathbf{p} \cdot \mathbf{k})(\mathbf{p} \cdot \hat{\mathbf{z}})}, \tag{3.9}$$

where \mathcal{F} is defined in (3.7) and (3.8) and involves the base state Ψ_0 . Integrating over all orientations and simplifying by \tilde{c}_0 yields

$$\int_{\Omega} \frac{\mathcal{F}}{\omega_0 + \lambda_2(\mathbf{p} \cdot \mathbf{k})(\mathbf{p} \cdot \hat{\mathbf{z}})} d\mathbf{p} = 1, \tag{3.10}$$

which is a dispersion relation for $\omega_0(k)$. Note that both flexibility and Brownian motion only enter this dispersion relation through the ratio of β and Pe appearing in the base state. In neglecting Pe^{-1} and β^{-1} in the governing equation, we have assumed that the correct order has been maintained with respect to the magnitude of perturbation in the linearized equation (3.1).

3.3.1. The isotropic base state

Before delving into the general case of the anisotropic base state of (2.15), we first revisit the limit of perfectly rigid rods ($\beta^{-1} = 0$) in the absence of thermal diffusion ($Pe^{-1} = 0$). This isotropic limit, formally reached by letting $\eta \rightarrow 0$ in (3.10), was previously explored by Koch & Shaqfeh (1989), Saintillan *et al.* (2006a) and Hoffman & Shaqfeh (2009) and will provide us with a reference point with which to compare the effects of flexibility and Brownian motion. In this case, the base state is simply $\Psi_0 = (4\pi)^{-1}$, and the dispersion relation (3.10) simplifies to

$$\frac{3\mathcal{N}}{4\pi k^2} \int_{\Omega} \frac{(\mathbf{p} \cdot \mathbf{k})(\mathbf{p} \cdot \hat{\mathbf{z}})}{\omega_0 + \lambda_2(\mathbf{p} \cdot \mathbf{k})(\mathbf{p} \cdot \hat{\mathbf{z}})} d\mathbf{p} = 1. \tag{3.11}$$

A numerical solution for $\omega_0(k)$ was first obtained by Koch & Shaqfeh (1989) and showed that the growth rate is maximum at $k = 0$ and decays monotonically with increasing wavenumber to reach zero at a critical wavenumber k_m , defining the marginal stability limit and indicating the range of unstable wavenumbers. Clearly, setting $\omega_0 = 0$ in (3.11) gives $k_m = \sqrt{3\mathcal{N}/\lambda_2}$. An approximation to $\omega_0(k)$ in the limit of small wavenumber can also be obtained by expanding (3.11) with error $O(k^4)$,

$$\begin{aligned} \frac{3\mathcal{N}}{4\pi\omega_0 k^2} \int_{\Omega} (\mathbf{p} \cdot \mathbf{k})(\mathbf{p} \cdot \hat{\mathbf{z}}) \left[1 - \frac{\lambda_2}{\omega_0} (\mathbf{p} \cdot \mathbf{k})(\mathbf{p} \cdot \hat{\mathbf{z}}) + \frac{\lambda_2^2}{\omega_0^2} (\mathbf{p} \cdot \mathbf{k})^2 (\mathbf{p} \cdot \hat{\mathbf{z}})^2 \right. \\ \left. - \frac{\lambda_2^3}{\omega_0^3} (\mathbf{p} \cdot \mathbf{k})^3 (\mathbf{p} \cdot \hat{\mathbf{z}})^3 + O(k^4) \right] d\mathbf{p} = 1. \end{aligned} \tag{3.12}$$

Now, recall that $\mathbf{p} = (\sin \theta \cos \varphi, \sin \theta \sin \varphi, \cos \theta)$ and that we have assumed a plane-wave perturbation in a direction perpendicular to gravity. In this case, the only dependence on the azimuthal angle φ comes from $\mathbf{p} \cdot \hat{\mathbf{k}} = \sin \theta \cos \varphi$. Noting that

$$\int_0^{2\pi} (\mathbf{p} \cdot \hat{\mathbf{k}})^2 d\varphi = \pi \sin^2 \theta, \quad \int_0^{2\pi} (\mathbf{p} \cdot \hat{\mathbf{k}})^4 d\varphi = \frac{3\pi}{4} \sin^4 \theta, \quad \int_0^{2\pi} (\mathbf{p} \cdot \hat{\mathbf{k}})^{2m+1} d\varphi = 0, \tag{3.13a-c}$$

for all $m \in \mathbb{Z}$, it follows that all terms in odd powers of k are zero in (3.12), which becomes

$$\omega_0^2 = -\frac{3\mathcal{N}\lambda_2}{4} \int_{-1}^1 u^2(1-u^2) du - \frac{9\mathcal{N}\lambda_2^3 k^2}{16\omega_0^2} \int_{-1}^1 u^4(1-u^2)^2 du + O(k^4), \tag{3.14}$$

and can be simplified to

$$\omega_0^2 = -\frac{\mathcal{N}\lambda_2}{5} + \frac{\mathcal{N}\lambda_2^2 k^2}{7} + O(k^4). \tag{3.15}$$

This readily provides the zero-wavenumber growth rate through the complex frequency $\omega_0 = \pm i\omega_m = \pm i\sqrt{\mathcal{N}\lambda_2/5}$. Recall the definitions $k^* = k/k_m$ and $\sigma = \omega_l/\omega_m$ for the scaled wavenumber and scaled growth rate, respectively. Restricting our attention to positive solutions for the growth rate, as only these drive the instability, we can recast the solution (3.15) for ω_0 with this scaling as

$$\sigma = 1 - \frac{15}{14}k^{*2} + O(k^{*4}). \tag{3.16}$$

3.3.2. *The perfectly aligned base state*

Another interesting limiting case is realized when $\eta \gg 1$, corresponding to a base state where the filaments are perfectly aligned in directions perpendicular to gravity. We have seen that any amount of flexibility introduces a rotational velocity that favours such an alignment, so this situation is relevant to the case of negligible diffusion ($Pe \rightarrow \infty$). The limiting base state is then readily shown to be $\Psi_0(\theta) = \delta(\theta - \pi/2)/2\pi$, where δ is the one-dimensional Dirac delta function. Inserting Ψ_0 into (3.7) for \mathcal{F} and using the property of the Dirac delta function that

$$(\mathbf{I} - \mathbf{p}\mathbf{p}) \cdot \hat{\mathbf{z}} \cdot \nabla_p \delta = (\mathbf{I} - \mathbf{p}\mathbf{p}) \cdot \hat{\mathbf{z}} \cdot \hat{\boldsymbol{\theta}} \delta' = -\sin \theta \delta', \tag{3.17}$$

where $\delta' = d\delta/d\theta$, we rewrite the dispersion relation (3.10) as

$$\frac{2\pi k^2}{\mathcal{N}} = \int_{\varphi=0}^{2\pi} \int_{\theta=0}^{\pi} \frac{k \sin^3 \theta \cos \varphi \delta'(\theta - \pi/2)}{\omega_0 + \lambda_2 k \sin \theta \cos \theta \cos \varphi} d\theta d\varphi. \tag{3.18}$$

The integrals are easily performed after an integration by parts with respect to θ , allowing us to evaluate the complex frequency as

$$\omega_0(k) = \pm i\sqrt{\frac{1}{2}\mathcal{N}\lambda_2} = \pm i\sqrt{\frac{5}{2}} \omega_m, \tag{3.19}$$

which, surprisingly, is independent of k . In other words, the growth rate in the perfectly aligned case exceeds the maximum growth rate in the isotropic case by a factor of $\sqrt{5/2}$ regardless of the value of the wavenumber k . This supports our initial speculation schematically illustrated in figure 4(b,c) that the preferred base orientation of the fibres towards the horizontal plane due to flexibility reinforces their tendency to drift horizontally in response to a density wave perturbation, thereby feeding in to the growth of the instability.

3.3.3. The general anisotropic base state

We now analyse the approximate dispersion relation (3.10) for the general anisotropic base state found in (2.15), written under the current non-dimensionalization as $\Psi_0(\theta) = m_0 \exp[-\eta \cos(2\theta)]$, where we recall that $\eta = A Pe / 4\lambda_3\beta$. The degree of anisotropy is set by the value of η , and the two limits $\eta \rightarrow 0$ (isotropic base state) and $\eta \rightarrow \infty$ (perfectly aligned base state) have already been examined. First, we insert (3.8) into (3.10) and note the following divergence theorem for a vector field \mathbf{w} in orientational space Ω , as derived in appendix B:

$$\int_{\Omega} \nabla_p \cdot \mathbf{w} \, d\mathbf{p} = 2 \int_{\Omega} \mathbf{p} \cdot \mathbf{w} \, d\mathbf{p}. \tag{3.20}$$

The integrand can then be expanded for $k \rightarrow 0$, and once again terms involving odd powers of k contain odd functions of the azimuthal angle φ and do not contribute. We find

$$\frac{\omega_0^2}{\mathcal{N}\lambda_2} = - \int_{\Omega} \Psi_0(\mathbf{p} \cdot \hat{\mathbf{k}})^2 [1 - (\mathbf{p} \cdot \hat{\mathbf{z}})^2] \left[1 + \frac{3\lambda_2^2 k^2}{\omega_0^2} (\mathbf{p} \cdot \hat{\mathbf{k}})^2 (\mathbf{p} \cdot \hat{\mathbf{z}})^2 \right] d\mathbf{p} + O(k^4). \tag{3.21}$$

Using the change of variables $u = \mathbf{p} \cdot \hat{\mathbf{z}} = \cos \theta$, the above integrals can be evaluated analytically. After normalizing the imaginary part of the eigenvalue by ω_m and the wavenumber by k_m , we obtain the following expansion for the growth rate in the long-wave limit:

$$\sigma(\eta) = \sqrt{\frac{5}{2}} J_1^{1/2} - \frac{27\sqrt{10}}{8} \frac{J_2}{J_1^{3/2}} k^{*2} + O(k^{*4}). \tag{3.22}$$

Here $J_1(\eta)$ and $J_2(\eta)$ denote the following functions:

$$J_1(\eta) = \frac{\int_{-1}^1 e^{-2\eta u^2} (1 - u^2)(1 - 2u^2) \, du}{\int_{-1}^1 e^{-2\eta u^2} \, du} = \frac{2\eta - 3}{2\sqrt{2\pi\eta^3}} \frac{e^{-2\eta}}{\text{erf}(\sqrt{2\eta})} + \frac{8\eta^2 - 6\eta + 3}{8\eta^2} \tag{3.23}$$

and

$$\begin{aligned} J_2(\eta) &= \frac{\int_{-1}^1 e^{-2\eta u^2} u^2(1 - u^2)^2(1 - 2u^2) \, du}{\int_{-1}^1 e^{-2\eta u^2} \, du} \\ &= \frac{8\eta^2 - 10\eta + 105}{32\sqrt{2\pi\eta^7}} \frac{e^{-2\eta}}{\text{erf}(\sqrt{2\eta})} + \frac{32\eta^3 - 96\eta^2 + 150\eta - 105}{128\eta^2}. \end{aligned} \tag{3.24}$$

In the limit of $\eta \rightarrow 0$, we expect to retrieve the results from our discussion of the isotropic base state in § 3.3.1. Indeed, we find that $J_1(0) = 2/5$ and $J_2(0) = 8/315$, which reduces (3.22) to (3.16). On the other hand, the limit of $\eta \rightarrow \infty$ corresponds to the perfectly aligned base state, and here we have $J_1(\infty) = 1$ and $J_2(\infty) = 0$, recovering (3.19). The monotonic behaviour of $J_1(\eta)$ further suggests that the

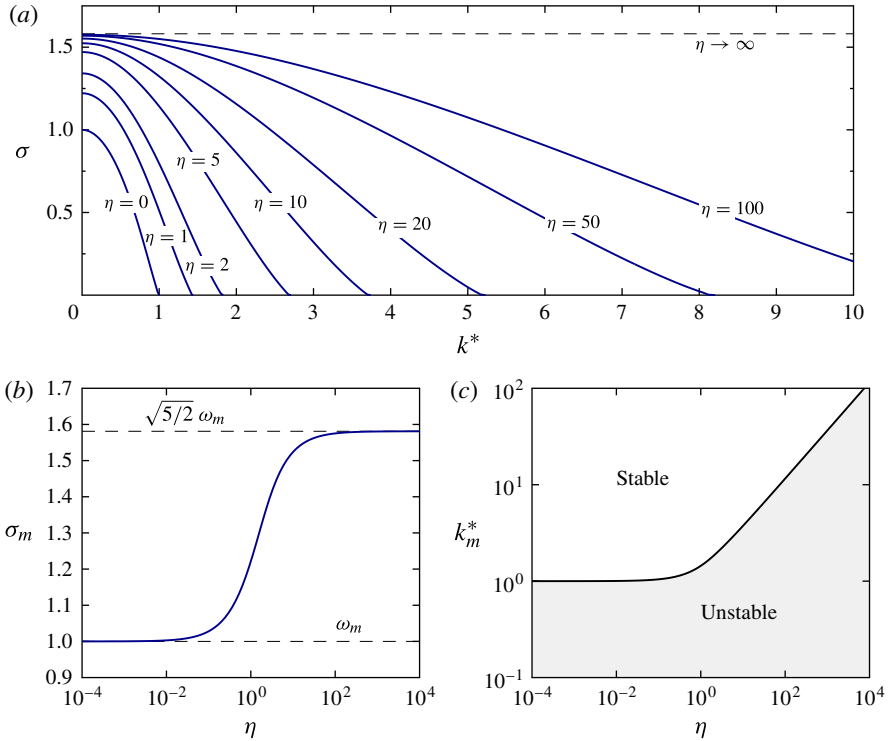


FIGURE 5. (Colour online) (a) Numerical solution to the dispersion relation (3.25) for various values of η . The limiting case $\eta = 0$ corresponds to the isotropic base state discussed in § 3.3.1, whereas $\eta \rightarrow \infty$ corresponds to the perfectly aligned base state of § 3.3.2. (b) Zero-wavenumber (maximum) growth rate as a function of η following (3.22). (c) Range of unstable wavenumbers as a function of η following (3.27).

maximum growth rate $\sigma_m(\eta) = \sigma(\eta; k = 0)$ is bounded between 1 as $\eta \rightarrow 0$ as we expect from the isotropic case and $\sqrt{5/2}$ as $\eta \rightarrow \infty$ as predicted earlier for the perfectly aligned case. The $O(k^{*2})$ correction to σ in (3.22) captures the change in the growth rate as we depart from the long-wave limit. As $\eta \rightarrow 0$, this correction asymptotes to $-15/14$ as predicted by (3.16). Further, it approaches zero for large η , consistent with the prediction of (3.19) that the growth rate in the perfectly aligned case takes the constant value of $\sqrt{5/2}$ independent of wavenumber.

The zero-wavenumber growth rate $\sigma_m = \sigma(\eta; k = 0)$ following (3.22) is plotted in figure 5(b) and is overlaid upon the full spectral solution data in figure 3(b), where we see that for $\beta \gg 1$ the effects of Brownian motion and flexibility occur almost exclusively through their influence on the base state, rather than through the terms of order Pe^{-1} and β^{-1} in (3.6), which were neglected when deriving (3.22) above. Therefore, the instability is predominantly affected by the anisotropy of the base state in this regime. The departure from the above prediction as seen in figure 3(b) for large values of η is the result of these terms coming into play, and this suppressive effect of diffusion and flexibility will be considered in § 3.4.

The dependence of the zero-growth-rate wavenumber on η may be calculated by seeking the value of k for which $\omega_0 = 0$. For this, we use (3.7) and note that

$\nabla_p \Psi_0 = -4u\eta\Psi_0(\mathbf{I} - \mathbf{p}\mathbf{p}) \cdot \hat{\mathbf{z}}$ to rewrite the dispersion relation (3.10) as

$$\frac{\mathcal{N}}{k^2} \int_{\Omega} \frac{\Psi(\mathbf{p} \cdot \mathbf{k})(\mathbf{p} \cdot \hat{\mathbf{z}})[3 + 4\eta(1 - (\mathbf{p} \cdot \hat{\mathbf{z}})^2)]}{\omega_0 + \lambda_2(\mathbf{p} \cdot \mathbf{k})(\mathbf{p} \cdot \hat{\mathbf{z}})} d\mathbf{p} = 1. \tag{3.25}$$

Letting $\omega_0 = 0$, this simplifies to

$$\frac{k^2 \lambda_2}{\mathcal{N}} = 3 + 4\eta \frac{\int_{-1}^1 e^{-2\eta u^2} (1 - u^2) du}{\int_{-1}^1 e^{-2\eta u^2} du}, \tag{3.26}$$

where the case of $\eta = 0$ yields the value of k_m obtained previously in the isotropic case. The integrals can be evaluated, and after scaling by k_m we express the zero-growth-rate wavenumber as

$$k_m^*(\eta) = \left[1 + \frac{4}{3} \sqrt{\frac{\eta}{2\pi}} \frac{e^{-2\eta}}{\text{erf}(\sqrt{2\eta})} + \frac{4\eta - 1}{3} \right]^{1/2}. \tag{3.27}$$

The range of unstable wavenumbers is shown in figure 5(c), and is found to grow without bound as $\sqrt{\eta}$ for large η (which, at a fixed value of the Péclet number, corresponds to increasing elastic flexibility of the filament backbones). Of course, we recall that values of η are limited by the underlying assumptions of the micromechanical model in § 2.1, which is only valid for relatively stiff filaments ($\beta \gtrsim 1$). Another limitation also exists on the value of k^{-1} , which must be much greater than the particle length: under the present non-dimensionalization, this restricts the validity of the solution to $k^* \lesssim \sqrt{\lambda_2/3\mathcal{N}}$.

A full solution to the dispersion relation (3.10) for arbitrary k cannot be obtained analytically. However, we solve it numerically using an end-corrected trapezoidal quadrature and a secant method to find the roots, and the solution $\omega_0(k)$ is shown for different values of η in figure 5(a). In agreement with the previous analyses, we recover the case of isotropically oriented rigid rods as $\eta \rightarrow 0$, whereas increasing η causes both the range of unstable wavenumbers and the value of the growth rate to increase. In the limit of $\eta \rightarrow \infty$, the solution asymptotes to the constant value of $\sigma = \sqrt{5/2}$ for a perfectly aligned suspension.

3.4. Direct effect of flexibility and Brownian motion

We now turn our attention to the direct effect of flexibility and Brownian motion through the terms of order β^{-1} and Pe^{-1} in the eigenvalue problem (3.6), which were previously neglected in the discussion of § 3.3. Hoffman & Shaqfeh (2009) previously analysed the effect of Brownian motion in the case of rigid rods, and found that it stabilizes the suspension by randomizing orientations. On the other hand, flexibility causes reorientation perpendicular to gravity. This reorientation competes against alignment by the disturbance flow and is now expected to suppress the instability. This is indeed observed in the spectral solution presented in figure 6: for a given value of η (i.e. for a given base-state distribution), we found that increasing flexibility causes a decrease in the maximum growth rate below the prediction of (3.25) for the base-state effect, as a result of the independent contribution of the $O(\beta^{-1})$ terms in the linearized equation (3.6).

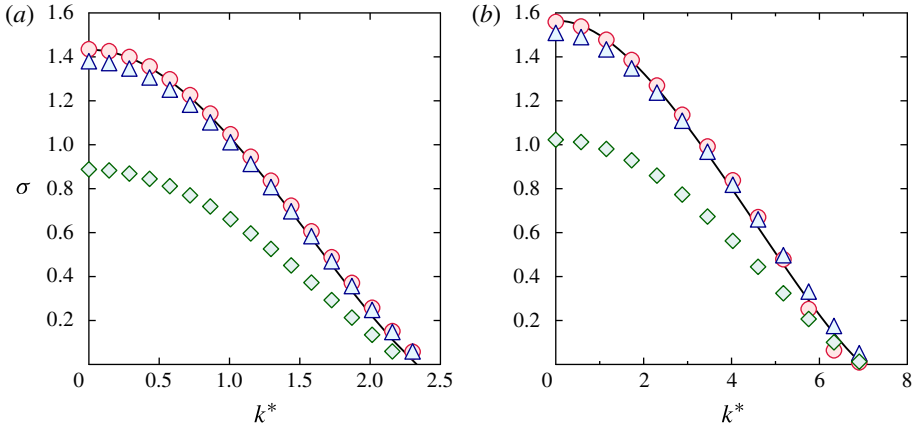


FIGURE 6. (Colour online) Suppression of the instability due to fibre flexibility for fixed η : (a) $\eta = 3.68$ and (b) $\eta = 36.68$. The symbols denote the spectral solutions for: (a) $\beta = 0.1, Pe = 10^3$ (\diamond); $\beta = 1, Pe = 10^4$ (\triangle); $\beta = 10, Pe = 10^5$ (\circ); and (b) $\beta = 0.1, Pe = 10^4$ (\diamond); $\beta = 1, Pe = 10^5$ (\triangle); $\beta = 10, Pe = 10^6$ (\circ). The solid line in each panel is the prediction for the effect of the base state alone, following (3.25). The suppression of the growth rate as β decreases (i.e. the filaments are made more flexible) is clear.

It is useful to remember that, for a fixed value of η , specifying either Pe or β implicitly defines the other. This suggests that the terms capturing the direct effects of Brownian motion and flexibility in (3.6) can be expressed in terms of only one parameter when η is given. In the subsequent analysis, we choose to use Pe^{-1} as the expansion parameter, though exactly the same results could be obtained with the alternate choice of β^{-1} . Substituting $\beta^{-1} = (4\lambda_3\eta/A)Pe^{-1}$ into (3.6) lets us recast the eigenvalue problem as

$$\begin{aligned}
 & -i[\omega + \lambda_2(\mathbf{p} \cdot \mathbf{k})(\mathbf{p} \cdot \hat{\mathbf{z}})]\tilde{\psi} + i\mathcal{F}\tilde{c} + Pe^{-1}[\lambda_1k^2 + \lambda_2(\mathbf{p} \cdot \mathbf{k})^2]\tilde{\psi} \\
 & - \lambda_3Pe^{-1}\nabla_p \cdot [\nabla_p\tilde{\psi} - 2\eta\tilde{\psi}\sin(2\theta)\hat{\boldsymbol{\theta}}] = 0,
 \end{aligned}
 \tag{3.28}$$

where η is fixed and finite and Pe^{-1} is assumed to be small. It is worth reiterating here that we are considering the regime where the effects of Brownian motion and flexibility are weak and of comparable magnitude, i.e. both Pe and β are large. The eigenfunction and eigenvalue can then be expanded as

$$\tilde{\psi} = \tilde{\psi}_0 + Pe^{-1}\tilde{\psi}_1 + O(Pe^{-2}),
 \tag{3.29}$$

$$\omega = \omega_0 + Pe^{-1}\omega_1 + O(Pe^{-2}),
 \tag{3.30}$$

and substituted into (3.28). The leading-order terms follow (3.9), where Pe and β only affect the base state through their ratio appearing in Ψ_0 . The next order in Pe^{-1} then gives us

$$\omega_0\tilde{\psi}_1 + \omega_1\tilde{\psi}_0 + \lambda_2(\mathbf{p} \cdot \mathbf{k})(\mathbf{p} \cdot \hat{\mathbf{z}})\tilde{\psi}_1 - \mathcal{F}\tilde{c}_1 + i(\mathcal{G} - \mathcal{H}) = 0,
 \tag{3.31}$$

where we have defined

$$\mathcal{G} = [\lambda_1k^2 + \lambda_2(\mathbf{p} \cdot \mathbf{k})^2]\tilde{\psi}_0,
 \tag{3.32}$$

$$\mathcal{H} = \lambda_3\nabla_p \cdot [\nabla_p\tilde{\psi}_0 - 2\eta\tilde{\psi}_0\sin(2\theta)\hat{\boldsymbol{\theta}}].
 \tag{3.33}$$

This can be rearranged to read

$$\frac{\omega_0 + \lambda_2(\mathbf{p} \cdot \mathbf{k})(\mathbf{p} \cdot \hat{\mathbf{z}})}{\mathcal{F}} \tilde{\psi}_1 + \frac{\tilde{\psi}_0}{\mathcal{F}} \omega_1 - \tilde{c}_1 + i \frac{\mathcal{G} - \mathcal{H}}{\mathcal{F}} = 0. \tag{3.34}$$

A simple expression for the first-order correction ω_1 of the complex frequency due to Brownian motion is then easily obtained after multiplication of (3.34) by $\tilde{\psi}_0$ and integration over the sphere of orientations Ω :

$$\omega_1 = -i \frac{\int_{\Omega} \frac{(\mathcal{G} - \mathcal{H})\tilde{\psi}_0}{\mathcal{F}} d\mathbf{p}}{\int_{\Omega} \frac{\tilde{\psi}_0^2}{\mathcal{F}} d\mathbf{p}}, \tag{3.35}$$

where we have used (3.9) to cancel the first and third terms in (3.34).

We now proceed to evaluate each term in (3.35) in the long-wave limit. Using the leading-order equation (3.28) to substitute for $\tilde{\psi}_0$ and taking $\tilde{c}_0 = 1$ without loss of generality, we find that the denominator is

$$\int_{\Omega} \frac{\tilde{\psi}_0^2}{\mathcal{F}} d\mathbf{p} = \int_{\Omega} \frac{\mathcal{F}}{[\omega_0 + \lambda_2(\mathbf{p} \cdot \mathbf{k})(\mathbf{p} \cdot \hat{\mathbf{z}})]^2} d\mathbf{p}. \tag{3.36}$$

Following the same procedure as in § 3.3, we expand the right-hand side to $O(k^4)$ and integrate by parts using the divergence theorem (3.20) to obtain

$$\int_{\Omega} \frac{\tilde{\psi}_0^2}{\mathcal{F}} d\mathbf{p} = -\frac{\mathcal{N}\lambda_2}{\omega_0^3} \left[J_1(\eta) + \frac{3}{8} \left(\frac{\lambda_2}{\omega_0} \right)^2 J_2(\eta) k^2 \right] + O(k^4), \tag{3.37}$$

where $J_1(\eta)$ and $J_2(\eta)$ were previously defined in (3.23) and (3.24). In a similar fashion, we can evaluate the first part of the numerator as

$$\int_{\Omega} \frac{\mathcal{G}\tilde{\psi}_0}{\mathcal{F}} d\mathbf{p} = \int_{\Omega} \frac{[\lambda_1 k^2 + \lambda_2(\mathbf{p} \cdot \mathbf{k})^2]\mathcal{F}}{[\omega_0 + \lambda_2(\mathbf{p} \cdot \mathbf{k})(\mathbf{p} \cdot \hat{\mathbf{z}})]^2} d\mathbf{p} \tag{3.38}$$

$$= -\frac{\mathcal{N}\lambda_2}{\omega_0^3} \left[\lambda_1 K_1(\eta) + \frac{3\lambda_2}{4} K_2(\eta) \right] k^2 + O(k^4), \tag{3.39}$$

where the two functions $K_1(\eta)$ and $K_2(\eta)$ are given by

$$K_1(\eta) = \frac{\int_{-1}^1 e^{-2\eta u^2} u^2(1-u^2)(4\eta(1-u^2)+3) du}{\int_{-1}^1 e^{-2\eta u^2} du} \tag{3.40}$$

and

$$K_2(\eta) = \frac{\int_{-1}^1 e^{-2\eta u^2} u^2(1-u^2)^2(4\eta(1-u^2)+3) du}{\int_{-1}^1 e^{-2\eta u^2} du}. \tag{3.41}$$

Finally, after integration by parts, the second part of the numerator becomes

$$\int_{\Omega} \frac{\mathcal{H}\tilde{\psi}_0}{\mathcal{F}} d\mathbf{p} = -\lambda_3 \int_{\Omega} [\nabla_p \tilde{\psi}_0 - 2\eta \tilde{\psi}_0 \sin(2\theta) \hat{\boldsymbol{\theta}}] \cdot \nabla_p \left[\frac{1}{\omega_0 + \lambda_2(\mathbf{p} \cdot \mathbf{k})(\mathbf{p} \cdot \hat{\mathbf{z}})} \right] d\mathbf{p}. \tag{3.42}$$

We substitute again for $\tilde{\psi}_0$ from the leading-order equation, and integrate an expansion in small k . All calculations done, this yields

$$\int_{\Omega} \frac{\mathcal{H}\tilde{\psi}_0}{\mathcal{F}} d\mathbf{p} = \frac{\mathcal{N} \lambda_2 \lambda_3}{2\omega_0^3} \left[L_1(\eta) + \left(\frac{\lambda_2}{\omega_0} \right)^2 L_2(\eta) k^2 \right] + O(k^4), \tag{3.43}$$

where $L_1(\eta)$ and $L_2(\eta)$ are defined as

$$L_1(\eta) = \int_{-1}^1 e^{-2\eta u^2} [-(24\eta + 12)u^2(1 - u^2) + (4\eta + 3)(1 + u^2) - 4\eta(u^2 + u^4) + 32\eta(1 - u^2)u^4] du \Big/ \int_{-1}^1 e^{-2\eta u^2} du \tag{3.44}$$

and

$$L_2(\eta) = \int_{-1}^1 e^{-2\eta u^2} \left\{ -(156\eta + 90)u^4(1 - u^2)^2 + 10(4\eta + 3) \left[u^4(1 - u^2) + \frac{3}{4}u^2(1 - u^2)^2 \right] - 40\eta \left[(1 - u^2)u^6 + \frac{3}{4}(1 - u^2)^2u^4 \right] + 192\eta(1 - u^2)^2u^6 \right\} du \Big/ \int_{-1}^1 e^{-2\eta u^2} du. \tag{3.45}$$

We now have all the ingredients to estimate the correction to the growth rate. Substituting (3.37), (3.39) and (3.43) into (3.35), we obtain an approximation for the correction to the eigenvalue in the limit of low wavenumbers:

$$\omega_1 = -i \frac{\lambda_3 L_1}{2 J_1} - ik^2 \left[-\frac{\lambda_2 \lambda_3 L_2}{\mathcal{N} J_1^2} + \frac{\lambda_1 K_1}{J_1} + \frac{3\lambda_2 K_2}{4 J_1} + \frac{3\lambda_2 \lambda_3 L_1 J_2}{8\mathcal{N} J_1^3} \right] + O(k^4). \tag{3.46}$$

The stabilizing effect of Brownian motion is best illustrated in the long-wavelength limit. At $k = 0$, the growth rate is given by

$$\sigma_m^{Pe}(Pe; \eta) = \sigma_m - \frac{\lambda_3 L_1}{2\omega_m J_1} Pe^{-1} + O(Pe^{-2}), \tag{3.47}$$

where we have again normalized with respect to the isotropic rigid-rod limit of ω_m . The subscript m indicates that this is the maximum growth rate reached in the long-wave limit, and σ_m is the base-state effect following (3.22) evaluated at $k = 0$. Equation (3.47) captures the leading correction to the growth rate due to thermal diffusion, and is compared to the spherical harmonics solution to the full eigenvalue problem in figure 7. As expected, Brownian motion leads to the randomization

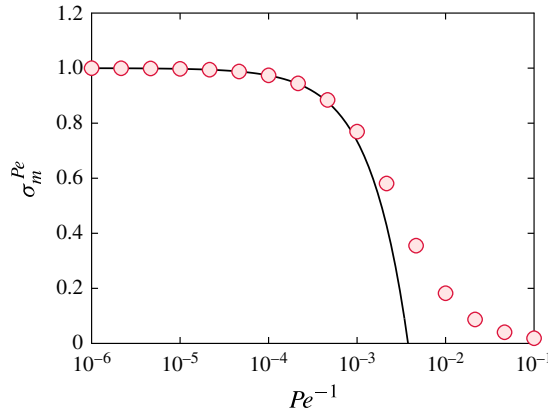


FIGURE 7. (Colour online) Suppression of the growth rate due to Brownian motion. The solid line shows the leading-order correction to the maximum growth rate as obtained in (3.47). The symbols are spectral solutions of the full eigenvalue problem obtained using spherical harmonics, all for $\beta = 10^6$.

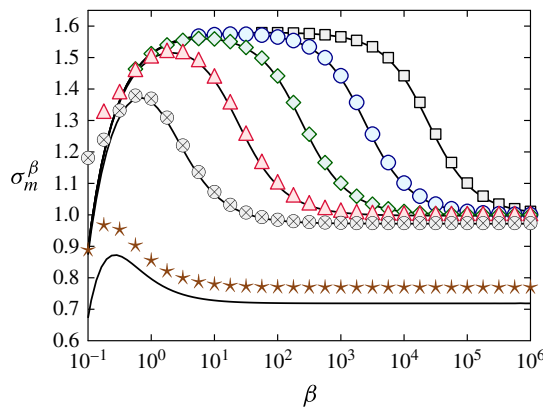


FIGURE 8. (Colour online) Suppression of the growth rate due to fibre flexibility. The solid line shows the leading-order correction to the maximum growth rate as obtained in (3.48). The symbols are spectral solutions of the full eigenvalue problem obtained using spherical harmonics for different Péclet numbers: $Pe = 10^8$ (\square), 10^7 (\circ), 10^6 (\diamond), 10^5 (\triangle), 10^4 (\otimes) and 10^3 (\star). The self-similar behaviour continues as low as $Pe \sim 10^4$, beyond which diffusion independently suppresses the growth rate.

of individual particle orientations and hence stabilizes the suspension. A similar conclusion was reached by Hoffman & Shaqfeh (2009), who considered the effect of Brownian motion on a suspension of polarizable rods placed in an electric field and also derived an expression similar to (3.22) in the simpler case of an isotropic base state.

As we explained earlier, Pe and β are interchangeable for a given value of η up to a constant factor depending on particle shape. Within the framework of the asymptotic expansion above, it is therefore possible to rewrite (3.47) in terms of β as

$$\sigma_m^\beta(\beta; \eta) = \sigma_m - \frac{A}{8\omega_m\eta} \frac{L_1}{J_1} \beta^{-1} + O(\beta^{-2}), \tag{3.48}$$

providing the leading effect of flexibility on the growth rate. This expression is shown to compare excellently with the numerical solution to the full eigenvalue problem in figure 8. Once again, it should be kept in mind that the asymptotic expansion is valid for $\beta \gtrsim 1$, and (3.48) does an excellent job of predicting the behaviour as the direct effect of flexibility becomes significant. The dual effect of flexibility is now obvious. On the one hand, we saw in §3.3 that it creates a base state that is more prone to instability, and this effect is the dominant one for stiff filaments. On the other hand, at the next order flexibility causes alignment of the filaments perpendicular to gravity in a way that hinders their rotation in the disturbance flow and therefore suppresses the growth rate. In the limit of large η , L_1/J_1 asymptotes to 4η . This means that the correction due to flexibility in (3.48) above goes like β^{-1} as flexibility becomes more important. The suppression of the growth rate as seen in figure 8 then becomes independent of η for sufficiently small values of β , which explains the collapse of all the curves corresponding to different values of Pe onto a single one. Finally, recall that the expansion is still first order in Pe^{-1} , and this means that the prediction becomes less accurate as rotational diffusion becomes stronger as was observed in figure 7. The same is the case again in figure 8 where the spectral solution departs slightly from the prediction for the smallest value of Péclet number shown.

3.5. *Effect of flexibility in the perfectly aligned state*

Finally, we also analyse the effect of flexibility in the perfectly aligned state (absent Brownian motion), with the base orientation distribution given by $\Psi_0 = \delta(\theta - \pi/2)/2\pi$ corresponding to fibres aligned perpendicular to gravity. As seen in (3.48), by letting $\eta \rightarrow \infty$, the direct effect of flexibility at first order is to reduce the zero-wavenumber growth rate by the value $A/(2\omega_m\beta)$. However, thanks to the special form of the base-state distribution in this case, we show here that we are in fact able to find the exact dispersion relation analytically for all permissible values of k and β . Two identities for the Dirac delta function $\delta(\theta - \pi/2)$ are useful in the derivation below:

$$h(\theta)\delta' = -h'(\pi/2)\delta + h(\pi/2)\delta', \tag{3.49}$$

$$h(\theta)\delta'' = h''(\pi/2)\delta - 2h'(\pi/2)\delta' + h(\pi/2)\delta''. \tag{3.50}$$

Inserting the expression for Ψ_0 into (3.8) for \mathcal{F} yields

$$\mathcal{F} = -\frac{\mathcal{N}}{k^2} \nabla_p \cdot [\Psi_0(\mathbf{p} \cdot \mathbf{k})(\mathbf{I} - \mathbf{p}\mathbf{p}) \cdot \hat{\mathbf{z}}] = \frac{\mathcal{N}}{2\pi k} \cos \varphi \delta'. \tag{3.51}$$

Upon inspection of the dispersion relation (3.6) in the limit of $Pe \rightarrow \infty$,

$$\{-i\omega - i\mathbf{k} \cdot (\lambda_1 \mathbf{I} + \lambda_2 \mathbf{p}\mathbf{p}) \cdot \hat{\mathbf{z}} + A\beta^{-1}(3 \cos^2 \theta - 1)\} \tilde{\psi} + \frac{A}{2\beta} \sin(2\theta) \frac{\partial \tilde{\psi}}{\partial \theta} + i\mathcal{F} \tilde{c} = 0, \tag{3.52}$$

we are led to consider the ansatz $\tilde{\psi} = f_1(\varphi)\delta(\theta - \pi/2) + f_2(\varphi)\delta'(\theta - \pi/2)$, so that (3.52) then reduces to

$$-(i\omega + A\beta^{-1})(f_1\delta + f_2\delta') - i\lambda_2 k \cos \varphi f_2\delta + \frac{A}{2\beta}(2f_1\delta + 4f_2\delta') + i\frac{\mathcal{N}}{2\pi k} \cos \varphi \tilde{c} \delta' = 0. \tag{3.53}$$

Expressions for f_1 and f_2 are determined without difficulty, and the eigenvalue problem is thus solved exactly. With the normalization requirement $\int_{\Omega} \tilde{\psi} \, d\mathbf{p} = \tilde{c}$, the exact formulae for the dispersion relation and the growth rate $\sigma = \omega_1/\omega_m$ are given by

$$\omega = -\frac{iA}{2\beta} \pm i\sqrt{\frac{A^2}{4\beta^2} + \frac{\lambda_2 \mathcal{N}}{2}}, \tag{3.54}$$

$$\sigma = -\frac{A}{2\omega_m\beta} \pm \sqrt{\frac{A^2}{4\omega_m^2\beta^2} + \frac{5}{2}}. \tag{3.55}$$

The $O(\beta^{-1})$ correction to the zero-wavenumber growth rate is $-A/(2\omega_m\beta)$, which agrees with the limit of $\eta \rightarrow \infty$ in (3.48). From this more complete expression, we see that the dispersion relation is independent of the wavelength of the horizontal perturbation in the perfectly aligned state as previously found in § 3.3.2 in the analysis of the effect of the base state.

Using the same approach, we can also obtain the dispersion relation for a more general initial perturbation with arbitrary wave direction $\hat{\mathbf{k}} = (\sin \alpha, 0, \cos \alpha)$ and find that

$$\omega = -\lambda_1 k \cos \alpha - \frac{iA}{2\beta} \pm i\sqrt{\frac{A^2}{4\beta^2} + \frac{\lambda_2 \mathcal{N} \sin^4 \alpha}{2}}. \tag{3.56}$$

For a perturbation wavevector parallel to gravity ($\alpha = 0$), (3.56) shows that ω is real, so the initial response of the suspension is a propagating density wave. Physically, the perturbation takes the form of regions of higher and lower fibre density layered in the direction of gravity, which travel vertically due to sedimentation. Instability only occurs when $\alpha \neq 0$, and in agreement with Koch & Shaqfeh (1989) we find that the maximum growth rate is achieved for a horizontal wave ($\alpha = \pi/2$). Equation (3.56) also shows that the growth rate is wavelength-independent even for non-horizontal perturbations, and perturbations of all wavelengths are therefore equally unstable in this case. To understand this curious result, we first note that the shear flow velocity set up by the initial perturbation scales as $\nabla_x \mathbf{u}_d \sim 1/k$. For small departures of fibre orientations from $\pi/2$, Jeffery’s equation (2.3) then gives $\dot{\mathbf{p}} \sim 1/k$. Then, since the horizontal translational velocity of the fibres due to their rotation in the flow scales approximately as $u_1 \sim 1/(k\omega)$, the conservation of particles $\partial_t c_1 \sim \partial_x(c_0 u_1)$ results in $\omega \sim 1/\omega$, indicating a growth rate independent of k . In other words, the larger sedimentation speed of particles in the more concentrated regions for higher-wavenumber perturbations balances the decreasing number of nearby fibres that are migrating into these regions.

4. Conclusion

We have investigated the effects of flexibility on the stability of a suspension of sedimenting fibres. Specifically, we considered the dynamics of weakly flexible fibres, characterized by large elasto-gravitation numbers, which are resistant to large deformations during the sedimentation process. In particular, we exploited two facts that are known about the sedimentation of isolated flexible filaments (Li *et al.* 2013): to leading order in the inverse elasto-gravitation number, a fibre translates with the same velocity as if it were a rigid rod and maintains a nearly straight shape as it sediments. We were therefore able to treat the suspension as one composed of rigid rods with the added ingredient of individual fibre reorientation during sedimentation.

We developed a mean-field model much akin to the one first described by Koch & Shaqfeh (1989), in which the probability density function describing the filament positions and orientations evolves according to a Smoluchowski equation. We first derived the statistical base state in the undisturbed and spatially homogeneous situation and found that it is in general anisotropic in the fibre orientation. In terms of a new variable η , which is a scaled ratio of the Péclet number to the elasto-gravitation number, the base state describes on one hand the isotropic distribution of rigid rods ($\eta = 0$), and on the other the perfectly aligned distribution that results when the suspension is athermal ($\eta \rightarrow \infty$). Speculating based on the mechanism that leads to an instability in the case of a suspension of rigid rods, we surmised that an anisotropic suspension composed of fibres oriented perpendicular to gravity would be more unstable to concentration fluctuations, owing to the fact that individual particles are more likely to be reoriented by the disturbance flow in a way that enhances the instability. This speculation was confirmed when we perturbed the governing equation about the base state and performed a linear stability analysis. The resulting eigenvalue problem is defined on the sphere of orientations, and admits a spectral solution on the basis of spherical harmonics. A numerical solution did indeed show that the system not only has a larger growth rate with increasing fibre flexibility, but also renders more wavenumbers unstable.

We then proceeded to examine separately the contributions of the anisotropic base state and of the direct effect of flexibility (or Brownian motion, which may be interpreted alternatively through the variable η). Expanding the eigenvalue problem in an asymptotic series in β^{-1} and Pe^{-1} , we first saw that the base state is almost entirely responsible for the enhancement of the instability, unless flexibility-induced reorientation is very strong. We showed that the growth rate increases monotonically with the variable η , continuously interpolating between the previously known value in the case of a suspension of isotropically distributed rigid rods to the limit of a perfectly aligned suspension where the growth rate is a factor of $\sqrt{5/2}$ faster. The range of unstable wavenumbers, too, was shown to grow with increasing values of η , and the window of instability in fact expands indefinitely as the suspension becomes more anisotropic.

Next, we derived the correction to the growth rate due to the terms of order β^{-1} and Pe^{-1} , thereby capturing the direct effect of flexibility and rotational diffusion – that which would be present even if not for the anisotropic base-state distribution. Since β and Pe are related through the variable η , flexible reorientation and rotational diffusion could both be studied simultaneously, and both effects were found to stabilize the suspension. These results confirmed intuition, as reorientation towards the direction perpendicular to gravity competes against rotation in the disturbance flow: this has the effect of preventing particles from migrating into already dense clusters and thereby suppresses the growth of the instability. Similarly, increased thermal motion randomizes fibre orientations and disrupts the mechanism that would entrain more particles into regions of higher concentration.

The results of this work are summarized in a phase diagram in figure 9. The phase boundaries are only to guide the eye, and the transitions are by no means sharp. The axes cover the range of β and Pe discussed here, as well as the pertinent range of the variable η . Contour lines of the maximum (zero-wavenumber) growth rate trace out regions where the growth rate is predicted to be negative, positive or greater than unity (which, under our normalization, is the case of a suspension of rigid rods). The entire phase space can be qualitatively divided into regions where one effect or the other becomes predominant. Here, (A) corresponds to the case of a base state that is

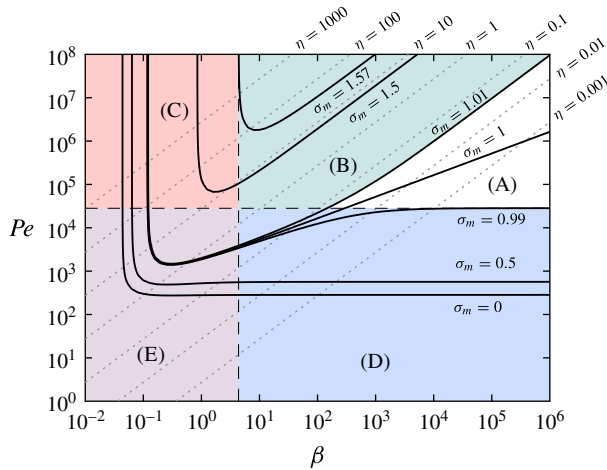


FIGURE 9. (Colour online) A summary of the effects of flexibility and diffusion on the stability of a suspension. The dotted lines denote the η co-ordinate, and solid lines are contours of the maximum growth rate σ_m at the indicated values. The dashed lines are meant to qualitatively divide the phase space into regions labelled (A)–(E): (A) negligible diffusion and fibre flexibility, and a near isotropic orientation distribution in the base state; the dynamics is indistinguishable from the case of a rigid-rod suspension. (B) Negligible direct effect of diffusion and fibre flexibility, although the base state is rendered anisotropic and a self-similar enhancement of the instability is seen. (C) Stabilization due to the direct effect of fibre-flexibility-induced reorientation. (D) Stabilization due to the direct effect of rotational diffusion. (E) Combined non-trivial effects of flexibility and Brownian motion.

nearly isotropic, and the independent effects of fibre flexibility and thermal fluctuations are negligible. We dealt with this in § 3.3.1 and saw that $\sigma_m = 1$ in this regime, and in figure 9 we concede a departure of ± 0.01 from unity to define this regime. Regime (B) is encountered as one departs from (A) along the η coordinate, and we saw in § 3.3.3 that this corresponds to the self-similar enhancement of the rigid-rod instability, solely due to the anisotropy of the base-state distribution. Particles preferentially align perpendicular to gravity, which increases their chance of migrating into dense regions as a result of hydrodynamic interactions, thereby enhancing the instability. Here, again, the independent effects of flexibility and Brownian motion are negligible. Increasing the fibre flexibility takes us to (C), where the independent effect of flexibility was shown in § 3.4 to be stabilizing. The propensity of individual particles to reorient perpendicular to gravity during sedimentation hinders their horizontal migration and thus stabilizes the suspension. Regime (D) depicts the regime where randomization due to thermal fluctuations suppresses the growth rate, which we named the direct effect of Brownian motion and analysed quantitatively in § 3.4. Finally, regime (E) is where the independent effects of both fibre flexibility and diffusion are significant and the observed stabilization cannot be individually attributed to either mechanism alone. Further, there are more regimes that can be identified and that are not shown in figure 9 for the sake of simplicity. For instance, near the border between (B) and (D) lies a region where the anisotropic base state enhances the instability but Brownian motion suppresses it.

We have assumed throughout that the base state has already been established, and restricted our attention to the linear stability of perturbations with respect to such

an orientation distribution. In a well-stirred suspension, particles can be assumed to be isotropically oriented, and it remains to be seen how the time over which such a base state is achieved compares with the growth rate of disturbances in an isotropically oriented suspension. Quantitatively, this is decided by the solution to an advection–diffusion equation in orientation space. Qualitatively, assuming weak diffusion, the base state is established on a time scale $|\dot{\mathbf{p}}_s|^{-1} \sim 2\beta/A$. Balancing this with the time scale ω_m^{-1} associated with the instability in an isotropic suspension, we find the condition $\mathcal{N} \lesssim A^2/\lambda_2\beta^2$ on the effective volume fraction of particles. This essentially states that the concentration has to be sufficiently low that hydrodynamic interactions do not hinder the establishment of the base state. The condition points to a very dilute suspension, which may require a very large container for the instability to be observed. Nevertheless, in a hypothetical infinite suspension, the instability does exist regardless of dilution since the maximum growth rate is achieved in the limit of $k \rightarrow 0$. Furthermore, the suppression of the instability due to individual particle reorientation (direct effect of flexibility) is expected to occur no matter whether the base-state distribution has been reached, and this effect can be relevant even in nearly isotropic suspensions.

In this work we have neglected the effect of the disturbance field on the shape of each fibre: strong interactions could potentially deform individual fibres from the assumed straight orientation, and change the settling dynamics. However, such detailed internal dynamics is not straightforward to describe in a mean-field kinetic model such as the one we have developed. Furthermore, it would seem to be a fair assumption that the diluteness of the suspension prevents particles from imposing strong disturbance fields upon one another. The same rationale applies to neglecting excluded-volume effects and steric interactions between fibres. Particle inertia, which we have neglected here as well, has been shown to eliminate growth at zero wavenumber (Dahlkild 2011) and could be relevant in rationalizing the formation of finite-sized vertical structures seen in experiments (Metzger *et al.* 2007). Particle simulations could hold the key to revealing microstructural changes and detailed internal dynamics in dilute as well as concentrated suspensions, and test the validity of our predictions as other physical effects become relevant. Further, while we have considered an infinite domain for analytical convenience, simulations could also lead the way in describing the effects of walls, which are known to become vital in real systems (Brenner 1999; Ladd 2002; Saintillan *et al.* 2006a). As a closing statement, we note that the stronger instability associated with the anisotropic base state described here is not necessarily exclusive to flexible fibres, and the approach used here can in principle apply to any suspension wherein a physical mechanism exists that causes orientable particles to align perpendicular to the direction of forcing.

Acknowledgements

D.S. gratefully acknowledges funding from NSF CAREER Grant No. CBET-1151590.

Appendix A. Spherical harmonics expansion

The full eigenvalue problem (3.6) is too complicated to be solved analytically in the general case owing to the additional terms arising from flexibility and thermal diffusion and to the non-trivial form of the base-state distribution (2.17). Instead, noticing that (3.6) is in the form $\mathcal{L}[\tilde{\psi}] = i\omega\tilde{\psi}$, where \mathcal{L} is a linear integro-differential operator, we seek numerical solutions to the eigenvalues ω by projecting $\tilde{\psi}$ onto an

appropriate basis. As $\tilde{\psi}$ is defined continuously on the sphere of orientations, a natural choice is Laplace's spherical harmonics,

$$Y_\ell^m(\theta, \varphi) = \sqrt{\frac{2\ell + 1}{4\pi} \frac{(\ell - m)!}{(\ell + m)!}} P_\ell^m(\cos \theta) e^{im\varphi}, \tag{A 1}$$

where P_ℓ^m are the associated Legendre polynomials. Projecting the unknown eigenfunctions onto this basis,

$$\tilde{\psi}(\theta, \varphi) = \sum_{\ell=0}^{\infty} \sum_{m=-\ell}^{\ell} a_{\ell m} Y_\ell^m(\theta, \varphi), \tag{A 2}$$

the linearity of the operator \mathcal{L} then implies that

$$\sum_{\ell=0}^{\infty} \sum_{m=-\ell}^{\ell} a_{\ell m} \mathcal{L}[Y_\ell^m] = i\omega \sum_{\ell=0}^{\infty} \sum_{m=-\ell}^{\ell} a_{\ell m} Y_\ell^m. \tag{A 3}$$

The spherical harmonics are orthonormal over the orientational space:

$$\langle Y_\ell^m, Y_{\ell'}^{m'} \rangle = \int_{\Omega} Y_\ell^m \bar{Y}_{\ell'}^{m'} d\mathbf{p} = \delta_{\ell\ell'} \delta_{mm'}, \tag{A 4}$$

where the overbar denotes the complex conjugate. Using this property, we multiply (A 3) by $\bar{Y}_{\ell'}^{m'}$ and integrate over all orientations to obtain

$$\sum_{\ell=0}^{\infty} \sum_{m=-\ell}^{\ell} a_{\ell m} \langle \mathcal{L}[Y_\ell^m], Y_{\ell'}^{m'} \rangle = i\omega a_{\ell' m'}. \tag{A 5}$$

Truncating the expansion at $\ell = M$ (where we choose $M = 30$ in the results presented here), (A 5) then yields an algebraic eigenvalue problem of the form $\mathbf{L} \cdot \mathbf{a} = i\omega \mathbf{a}$, where \mathbf{L} is an $(M + 1)^2 \times (M + 1)^2$ matrix with entries $\langle \mathcal{L}[Y_\ell^m], Y_{\ell'}^{m'} \rangle$ and the vector \mathbf{a} contains the coefficients $a_{\ell m}$ of the spectral expansion of the eigenfunction. Solving this system provides a discrete set of $(M + 1)^2$ eigenvalues ω . We verify *a posteriori* that only one of these eigenvalues is unstable ($\omega_r > 0$), consistent with the results of Koch & Shaqfeh (1989).

The following properties of spherical harmonics are useful in evaluating the matrix \mathbf{L} :

$$\int_{\Omega} Y_\ell^m d\mathbf{p} = 2\sqrt{\pi} \delta_{\ell 0} \delta_{m 0}, \tag{A 6}$$

$$\nabla_p^2 Y_\ell^m = -\ell(\ell + 1) Y_\ell^m, \tag{A 7}$$

$$\frac{\partial Y_\ell^m}{\partial \theta} = \frac{1}{\sin \theta} \left(\ell \cos \theta Y_\ell^m - \sqrt{\frac{(2\ell + 1)(\ell^2 - m^2)}{2\ell - 1}} Y_{\ell-1}^m \right). \tag{A 8}$$

Appendix B. The divergence theorem in orientational space

The divergence theorem (3.20) in orientational space follows directly from Gauss's theorem. Let $\mathbf{w}(\mathbf{p})$ be any smooth function defined on the surface Ω of a unit sphere. We also define $\mathbf{v}(r, \mathbf{p}) = r^n \mathbf{w}$, where $n \geq 1$ to ensure regularity. Now, the unit ball is $B = \{r\Omega \mid 0 \leq r \leq 1\}$ and Gauss's divergence theorem reads

$$\int_B \nabla \cdot \mathbf{v} \, dV = \int_\Omega \mathbf{p} \cdot \mathbf{v} \, d\mathbf{p}. \quad (\text{B } 1)$$

Noticing that $\nabla = \mathbf{p} \partial / \partial r + (1/r) \nabla_p$, the left-hand side can be shown to be

$$\int_B (nr^{n-1} \mathbf{p} \cdot \mathbf{w} + r^{n-1} \nabla_p \cdot \mathbf{w}) \, dV = \int_\Omega \left(\frac{n}{n+2} \mathbf{p} \cdot \mathbf{w} + \frac{1}{n+2} \nabla_p \cdot \mathbf{w} \right) \, d\mathbf{p}, \quad (\text{B } 2)$$

where we have used $dV = r^2 \, dr \, d\mathbf{p}$. The right-hand side of (B 1) simplifies readily as $\mathbf{v} = \mathbf{w}$ on Ω . Rearranging the terms, we obtain the desired result.

REFERENCES

- BATCHELOR, G. K. 1972 Sedimentation in a dilute dispersion of spheres. *J. Fluid Mech.* **52**, 245–268.
- BERGOUNOUX, L., GHICINI, S., GUAZZELLI, E. & HINCH, J. 2001 Spreading fronts and fluctuations in sedimentation. *Phys. Fluids* **15**, 1875–1887.
- BIRD, R. B., ARMSTRONG, R. C. & HASSAGER, O. 1987 *Dynamics of Polymeric Liquids*, vol. I, *Fluid Mechanics*. Wiley Interscience.
- BRENNER, M. P. 1999 Screening mechanisms in sedimentation. *Phys. Fluids* **11**, 754–772.
- BUTLER, J. E. & SHAQFEH, E. S. G. 2002 Dynamic simulations of the inhomogeneous sedimentation of rigid fibres. *J. Fluid Mech.* **468**, 205–237.
- CAFLISCH, R. E. & LUKE, J. H. C. 1985 Variance in the sedimentation speed of a suspension. *Phys. Fluids* **28**, 759–760.
- COSENTINO LAGOMARSINO, M., PAGONABARRAGA, I. & LOWE, C. P. 2005 Hydrodynamic induced deformation and orientation of a microscopic elastic filament. *Phys. Rev. Lett.* **94**, 148104.
- DAHLKILD, A. 2011 Finite wavelength selection for the linear instability of a suspension of settling spheroids. *J. Fluid Mech.* **689**, 183–202.
- DOI, M. & EDWARDS, S. F. 1986 *The Theory of Polymer Dynamics*. Oxford University Press.
- FAUCI, L. J. & DILLON, R. 2006 Biofluidmechanics of reproduction. *Annu. Rev. Fluid Mech.* **38**, 371–394.
- GAO, T., BLACKWELL, R., GLASER, M. A., BETTERTON, M. D. & SHELLEY, M. J. 2014 A multiscale active nematic theory of microtubule/motor-protein assemblies. ArXiv Preprint [arXiv:1401.8059](https://arxiv.org/abs/1401.8059).
- GARDEL, M. L., NAKAMURA, F., HARTWIG, J. H., CROCKER, J. C., STOSSEL, T. P. & WEITZ, D. A. 2006 Prestressed F-actin networks cross-linked by hinged filamins replicate mechanical properties of cells. *Proc. Natl Acad. Sci. USA* **103**, 1762–1767.
- GOUBAULT, C., JOP, P., FERMIGIER, M., BAUDRY, J., BERTRAND, E. & BIBETTE, J. 2003 Flexible magnetic filaments as micromechanical sensors. *Phys. Rev. Lett.* **91**, 260802.
- GROISMAN, A. & STEINBERG, V. 2000 Elastic turbulence in a polymer solution flow. *Nature* **405**, 53–55.
- GUAZZELLI, É. 2001 Evolution of particle-velocity correlations in sedimentation. *Phys. Fluids* **13**, 1537–1540.
- GUAZZELLI, É. & HINCH, J. 2011 Fluctuations and instability in sedimentation. *Annu. Rev. Fluid Mech.* **43**, 97–116.
- GUSTAVSSON, K. & TORNBERG, A.-K. 2009 Gravity induced sedimentation of slender fibres. *Phys. Fluids* **21**, 123301.

- HAM, J. M. & HOMSY, G. M. 1988 Hindered settling and hydrodynamic dispersion in quiescent sedimenting suspensions. *Intl J. Multiphase Flow* **14**, 533–546.
- HASIMOTO, H. 1959 On the periodic fundamental solutions to the Stokes equations and their application to viscous flow past a cubic array of spheres. *J. Fluid Mech.* **5**, 317–328.
- HERZHAFT, B., GUAZZELLI, É., MACKAPLOW, M. B. & SHAQFEH, E. S. G. 1996 Experimental investigation of the sedimentation of a dilute fibre suspension. *Phys. Rev. Lett.* **77**, 290–293.
- HINCH, E. J. 1987 Sedimentation of small particles. In *Disorder and Mixing* (ed. E. Guyon, J.-P. Nadal & Y. Pomeau), chap. 9, pp. 153–161. Kluwer.
- HOFFMAN, B. D. & SHAQFEH, E. S. G. 2009 The effect of Brownian motion on the stability of sedimenting suspensions of polarizable rods in an electric field. *J. Fluid Mech.* **624**, 361–388.
- JEFFERY, G. B. 1922 The motion of ellipsoidal particles immersed in a viscous fluid. *Proc. R. Soc. Lond. A* **102**, 161–179.
- KESHTKAR, M., HEUZEY, M. C. & CARREAU, P. J. 2009 Rheological behaviour of fibre-filled model suspensions: effect of fibre flexibility. *J. Rheol.* **53**, 631–650.
- KIM, S. & KARRILA, S. J. 2005 *Microhydrodynamics: Principles and Selected Applications*. Dover.
- KOCH, D. L. & SHAQFEH, E. S. G. 1989 The instability of a dispersion of sedimenting spheroids. *J. Fluid Mech.* **209**, 521–542.
- KOCH, D. L. & SHAQFEH, E. S. G. 1991 Screening in sedimenting suspensions. *J. Fluid Mech.* **224**, 275–303.
- KUUSELA, E., LAHTINEN, J. M. & ALA-NISSILA, T. 2003 Collective effects in settling of spheroids under steady-state sedimentation. *Phys. Rev. Lett.* **90**, 094502.
- LADD, A. J. C. 2002 Effects of container walls on the velocity fluctuations of sedimenting spheres. *Phys. Rev. Lett.* **88**, 048301.
- LAUGA, E. & POWERS, T. R. 2009 The hydrodynamics of swimming microorganisms. *Rep. Prog. Phys.* **72**, 096601.
- LI, L., MANIKANTAN, H., SAINTILLAN, D. & SPAGNOLIE, S. 2013 The sedimentation of flexible filaments. *J. Fluid Mech.* **735**, 705–736.
- LUKE, J. H. C. 2000 Decay of velocity fluctuations in a stably stratified suspension. *Phys. Fluids* **12**, 1619–1621.
- MACKAPLOW, M. B. & SHAQFEH, E. S. G. 1998 A numerical study of the sedimentation of fibre suspensions. *J. Fluid Mech.* **376**, 149–182.
- MANGA, M. & STONE, H. A. 1995 Collective hydrodynamics of deformable drops and bubbles in dilute low Reynolds number suspensions. *J. Fluid Mech.* **300**, 231–263.
- METZGER, B., BUTLER, J. E. & GUAZZELLI, E. 2007 Experimental investigation of the instability of a sedimenting suspension of fibres. *J. Fluid Mech.* **575**, 307–332.
- METZGER, B., GUAZZELLI, E. & BUTLER, J. E. 2005 Large-scale streamers in the sedimentation of a dilute fibre suspension. *Phys. Rev. Lett.* **95**, 164506.
- MUCHA, P. J. & BRENNER, M. P. 2003 Diffusivities and front propagation in sedimentation. *Phys. Fluids* **15**, 1305–1313.
- MUCHA, P. J., TEE, S.-Y., WEITZ, D. A., SHRAIMAN, B. I. & BRENNER, M. P. 2004 A model for velocity fluctuations in sedimentation. *J. Fluid Mech.* **501**, 71–104.
- NARSIMHAN, V. & SHAQFEH, E. S. G. 2010 Lateral drift and concentration instability in a suspension of bubbles induced by Marangoni stresses at zero Reynolds number. *Phys. Fluids* **22**, 101702.
- RAMASWAMY, S. 2001 Issues in the statistical mechanics of steady sedimentation. *Adv. Phys.* **50**, 297–341.
- SAINTEILLAN, D., DARVE, E. & SHAQFEH, E. S. G. 2005 A smooth particle-mesh Ewald algorithm for Stokes suspension simulations: the sedimentation of fibres. *Phys. Fluids* **17**, 033301.
- SAINTEILLAN, D., SHAQFEH, E. S. G. & DARVE, E. 2006a The effect of stratification on the wavenumber selection in the instability of sedimenting spheroids. *Phys. Fluids* **18**, 121503.
- SAINTEILLAN, D., SHAQFEH, E. S. G. & DARVE, E. 2006b The growth of concentration fluctuations in dilute dispersions of orientable and deformable particles under sedimentation. *J. Fluid Mech.* **553**, 347–388.
- SAINTEILLAN, D., SHAQFEH, E. S. G. & DARVE, E. 2006c Stabilization of a suspension of sedimenting rods by induced-charge electrophoresis. *Phys. Fluids* **18**, 121701.

- SAINTILLAN, D. & SHELLEY, M. J. 2012 Emergence of coherent structures and large-scale flows in motile suspensions. *J. R. Soc. Interface* **9**, 571–585.
- SEGRÈ, P. N., HERBOLZHEIMER, E. & CHAIKIN, P. M. 1997 Long-range correlations in sedimentation. *Phys. Rev. Lett.* **79**, 2574–2577.
- SWITZER, L. H. III & KLINGENBERG, D. J. 2003 Rheology of sheared flexible fibre suspensions via fibre-level simulations. *J. Rheol.* **47**, 759–778.
- TORNBERG, A.-K. & GUSTAVSSON, K. 2006 A numerical method for simulations of rigid fibre suspensions. *J. Comput. Phys.* **215**, 172–196.
- TORNBERG, A.-K. & SHELLEY, M. J. 2004 Simulating the dynamics and interactions of flexible fibres in Stokes flows. *J. Comput. Phys.* **196**, 8–40.
- VAN DEN HEUVEL, M., BONDESAN, R., LAGOMARSINO, M. C. & DEKKER, C. 2008 Single-molecule observation of anomalous electrohydrodynamic orientation of microtubules. *Phys. Rev. Lett.* **101**, 118301.
- VAN DER SCHOOT, P. 1996 The nematic–smectic transition in suspensions of slightly flexible hard rods. *J. Physique II* **6**, 1557–1569.
- VISHNAMPET, R. & SAINTILLAN, D. 2012 Concentration instability of sedimenting spheres in a second-order fluid. *Phys. Fluids* **24**, 073302.
- XU, X. & NADIM, A. 1994 Deformation and orientation of an elastic slender body sedimenting in a viscous liquid. *Phys. Fluids* **6**, 2889–2893.
- ZHANG, F., DAHLKILD, A. & LUNDELL, F. 2013 Nonlinear disturbance growth during sedimentation of dilute fibre suspensions. *J. Fluid Mech.* **719**, 268–294.
- ZINCHENKO, A. Z. & DAVIS, R. H. 2003 Large-scale simulations of concentrated emulsion flows. *Phil. Trans. R. Soc. Lond. A* **361**, 813–845.